Chapter 1

Abnormal Grain Growth Texture

Dong Nyung Lee and Sung Bo Lee

Additional information is available at the end of the chapter

http://dx.doi.org/10.5772/59724

1. Introduction

When the dislocation density in fabricated materials is not high enough to cause recrystallization, a theory for the texture evolution during recrystallization (the strain-energy-release maximization theory) [1] is not applicable. In this case, grain boundaries, free surfaces, and internal stresses can be sources of internal energy and will control the evolution of textures during annealing. For bulk materials, grain boundary energy dominates internal energy. For polycrystalline films, grain boundaries, surface, interface, and internal stress can be sources of internal energy. Minimization of all the energies can, in principle, determine the competition between the variously oriented and stressed growing grains, which in turn gives rise to the abnormal grain growth texture [2]. In this chapter, the evolution of abnormal grain growth textures in drawn silver and copper wires, nanocrystalline deposits such as Fe-Ni alloy electrodeposits, Ni electrodeposits, electroless Ni-P deposits, electroless Ni-Co-P deposits, electroless Ni-Cu-P deposits, and copper interconnects will be discussed. Textures of Al-1%Cu interconnects and annealing textures of nanocrystalline copper thin films will also be discussed.

2. The evolution of abnormal grain growth textures in drawn face-centered cubic (fcc) metals

2.1. Silver wire

The annealing textures of cold drawn silver wire were studied by Shin et al. [3]. The Rex textures of cold drawn silver wires were discussed in [1]. When annealed for 1 min at 600°C, a 99.99% pure silver wire cold-drawn by 99% reduction in area was almost completely recrystallized (Rexed). The Rex texture was composed of the <100>//AD component in the

majority and the <111>//AD component in the minority, where AD stands for the axial direction. However, as annealing time was prolonged, the <111>//AD component became higher than the <100>//AD component, and the orientation density ratio of <111>//AD to <100>//AD increases, accompanied by abnormal grain growth.

The texture change during grain growth after Rex must be related to grain boundary characteristics. In this stage, dislocation cannot influence the texture change because of its low density. The abnormal grain growth texture was discussed with reference to a theory developed by Abbruzzese and Lücke [4]. This theory allows to quantitatively take into account the influence of textures on grain growth. The theory is based on the statistical model of grain growth proposed by Hillert [5] and modified by Abbruzzese [6]. Shin et al. [3] considered a system composed of two major orientations, *A* and *B*, and other minor orientations, *C*. For the system, the growth rates of the *A*-, *B*-, and *C*-oriented grains of the size class *i* are expressed as [3]

$$\frac{dR_i^A}{dt} = \tilde{M}^A \left(\frac{1}{\tilde{R}_C^A} - \frac{1}{R_i^A} \right) \tag{1}$$

$$\frac{dR_i^B}{dt} = \tilde{M}^B \left(\frac{1}{\tilde{R}_C^B} - \frac{1}{R_i^B} \right) \tag{2}$$

$$\frac{dR_i^C}{dt} = \tilde{M}^C \left(\frac{1}{\tilde{R}_C^C} - \frac{1}{R_i^C} \right) \tag{3}$$

Here

$$\tilde{M}^A = \frac{\Phi^A \overline{R^2}^A M^{AA} + \Phi^B \overline{R^2}^B M^{AB} + \sum_C \Phi^C \overline{R^2}^C M^{AC}}{\Phi^A \overline{R^2}^A + \Phi^B \overline{R^2}^B + \sum_C \Phi^C \overline{R^2}^C} \tag{4}$$

$$\tilde{M}^B = \frac{\Phi^A \overline{R^2}^A M^{AB} + \Phi^B \overline{R^2}^B M^{BB} + \sum_C \Phi^C \overline{R^2}^C M^{BC}}{\Phi^A \overline{R^2}^A + \Phi^B \overline{R^2}^B + \sum_C \Phi^C \overline{R^2}^C} \tag{5}$$

$$\tilde{R}_C^A = \frac{\Phi^A \overline{R^2}^A M^{AA} + \Phi^B \overline{R^2}^B M^{AB} + \sum_C \Phi^C \overline{R^2}^C M^{AC}}{\Phi^A M^{AA} \overline{R}^A + \Phi^B M^{AB} \overline{R}^B + \sum_C \Phi^C M^{AC} \overline{R}^C} \tag{6}$$

http://dx.doi.org/10.5772/59724

$$\tilde{R}_C^B = \frac{\Phi^A \overline{R^2}^A M^{BA} + \Phi^B \overline{R^2}^B M^{BB} + \sum_C \Phi^C \overline{R^2}^C M^{BC}}{\Phi^A M^{BA} \overline{R}^A + \Phi^B M^{BB} \overline{R}^B + \sum_C \Phi^C M^{BC} \overline{R}^C} \tag{7}$$

$\bar{R}$ denotes the mean radius of all the grains and $\bar{R}^H$ that of the grains of texture component H. The different averages can be written as

$$\bar{R} = \sum_i \Phi_i R_i;\ \bar{R}^H = \sum_i \Phi_i^H R_i^H / \Phi^H \tag{8}$$

$$\overline{R^2} = \bar{R}^2 + \sigma^2 = \bar{R}^2(1+\kappa^2) \tag{9}$$

$$\overline{R^2}^H = \bar{R}^{H2} + \sigma^{H2} = \bar{R}^{H2}(1+\kappa^{H2}) \tag{10}$$

with $\Phi_i = \Phi_i^A + \Phi_i^B + \Phi_i^C$; $\Phi^A = \sum_i \Phi_i^A$; $\Phi^B = \sum_i \Phi_i^B$; $\Phi^C = \sum_i \Phi_i^C$ and $\Phi^A + \Phi^B + \Phi^C = 1$.

Φ_i^H denotes the number of grains per unit volume of class (i, H), n_i^H, divided by the total number of grains N_G, i.e.,

$\Phi_i^H = n_i^H / N_G$ with $\sum_H \sum_i n_i^H = N_G$;

$$\sum_H \sum_i \Phi_i^H = 1 \tag{11}$$

σ and σ^H are the standard deviations and $\kappa = \sigma / \bar{R}$ and $\kappa^H = \sigma^H / \bar{R}^H$ the variation coefficients. M^{AB}, the grain growth diffusivity of a boundary between grains of the orientations A and B, is defined as

$$M^{AB} = 2m^{AB}\gamma^{AB} \tag{12}$$

where m^{AB} and γ^{AB} are the mobility and the tension of the boundary between grains of the orientations A and B. It is usually assumed that $M^{AB} = M^{BA}$. According to Eq. 1, $\widetilde{M}^H$ and $\tilde{R}_C^H$, which denote integrated diffusivity and integrated critical radius for the texture component H, respectively, control the growth of component H. $\tilde{R}_C^H$ is the radius dividing the grain sizes of component H into those which grow and those which shrink, and $\widetilde{M}^H$ determines the rate

of these processes. Furthermore, a total critical radius R_C and the partial critical radii R_C^H are given by [3]

$$R_C = \overline{R^2} / \bar{R}; R_C^H = \overline{R^2}^H / \bar{R}^H \tag{13}$$

R_C corresponds to the critical radius of the grain size distribution if all M^{HK} would be equal (then all grains with $R_i > R_C$ would grow and those with $R_i < R_C$ would shrink), and R_C^H would be the critical radius if only the grains of the orientation H would exist [7]. If $M^{AA} > M^{ij}$ with $i \neq A$ and $j \neq A$, $\widetilde{M}^A > \widetilde{M}^B$ and $\widetilde{M}^A > \widetilde{M}^C$. Therefore, the grain growth rate in cluster of A grains is the highest, leading to elimination of the A–A boundary and thus an increase in size of the A grains. The resultant size advantage of A grains will cause the growth of A at the expense of neighboring B or C grains [3].

The recrystallized fcc metal wire has a fiber texture composed of major <100>//AD, minor <111>// AD, and others. The grain boundaries of wire can be approximated by tilt boundaries of <100>// AD, <111>//AD, and other grains, along with boundaries between them as shown in Figure 1. If the <111>//AD grain is denoted as A, the <100>//AD grains as B, and others as C, then the above discussion can be applied to the present system. In order for this theory to be applied, grain boundary mobility should be known. To the best of our knowledge, the grain boundary mobility data for silver are not available. However, the mobility data for aluminum indicate that the average mobility of <111> tilt boundary is much higher than that of <100> boundary at elevate temperatures above 400°C (Figure 2). If this tendency holds for the present system, since grain boundary energies are expected to be approximately same in average (Figures 3), A grains will grow at the expense of neighboring B or C grains, as already explained [3].

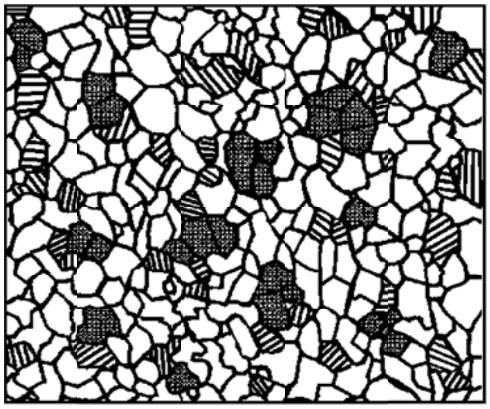

Figure 1. Schematic microstructure of section normal to wire axis, which consists of <100>//AD grains (white), <111>//AD grains (crosshatched), and grains having other orientations (hatched) [3].

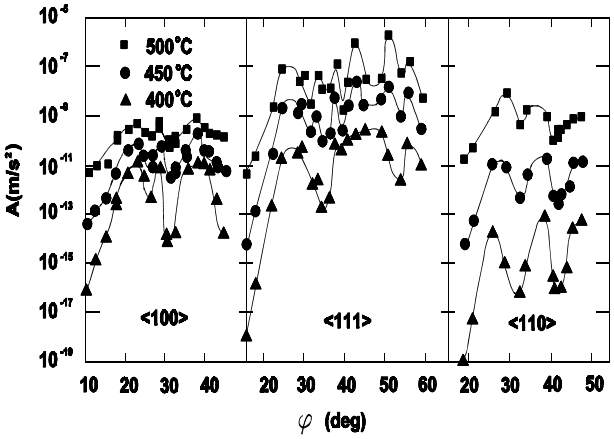

Figure 2. Misorientation dependence of tilt grain boundary mobility in aluminum of misorientation axes <100>, <110>, <111> [8].

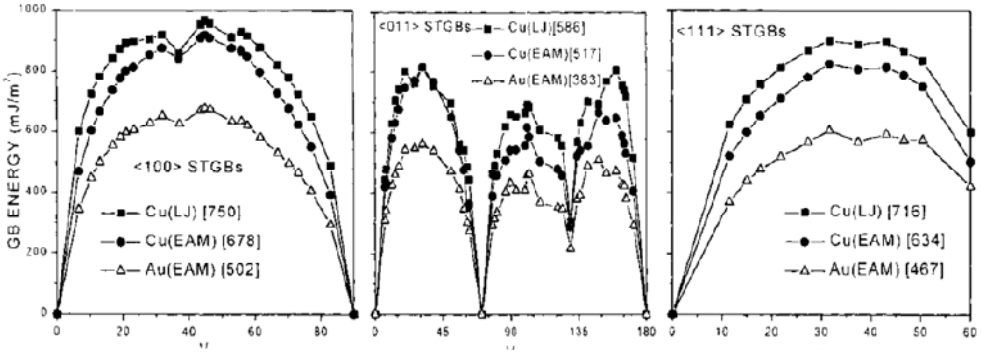

(a) (b) (c)

Figure 3. Calculated energy (in mJ/m^2) for symmetrical tilt grain boundaries of fcc metals with interface planes perpendicular to (a) <100>, (b) <110>, (c) <111> as a function of tilt angle. LJ and EAM indicate energies calculated using LJ and EAM potentials [9]. Quantity in brackets indicates average tilt boundary energy [3].

2.2. Copper wire

The global texture of drawn copper wires are characterized by the major <111>//AD + minor <100>//AD duplex fiber texture [10-13]. Annealing of the drawn copper wires at low temperatures leads to the development of the major <100>//AD + minor <111>//AD duplex fiber Rex texture [11-13]. Park and Lee [13] studied annealing textures of 90% drawn copper wires. The global deformation texture consisting of major <111>//AD + minor <100>//AD orientations changed to the major <100>//AD + minor <111>//AD texture, as shown in Figure 4, which shows the orientation density ratio of <100>//AD to <111>//AD in the drawn copper wire as a function

of annealing time at 700°C. The ratio increases steeply up to about 1.8 after annealing for 180 s, wherefrom it decreases and approach about 0.3 after 6 h [13]. The increase in the ratio indicates the occurrence of primary recrystallization [13] and the decrease demonstrates a change in texture during subsequent abnormal grain growth as can be seen in Figure 5. The figure shows optical microstructures of the drawn wires annealed at 700°C for times varying from 10 min to 6 h [13]. Abnormal grain growth takes place first near the surface and the grains grow into the center [13].

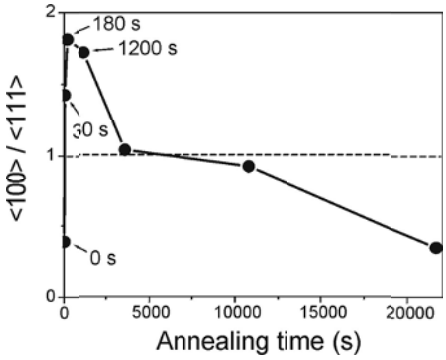

Figure 4. Orientation density ratio of <100>//AD to <111>//AD of 90% drawn copper wires as a function of annealing time at 700°C [13].

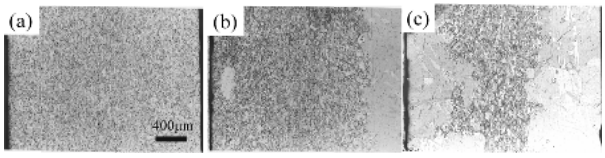

Figure 5. Optical microstructures of copper wires drawn by 90% and annealed at 700°C for (a) 10 min, (b) 1 h, (c) 6 h [13].

The grain size distribution along the radial direction of the longitudinal section of the drawn wire after annealing for 1 h at 700°C shows no considerable abnormal grain growth as shown in Figure 5. The average grain sizes and the size distributions of grains smaller than 2 $\bar{R}$, where $\bar{R}$ stands for the average grain size, were similar in all regions [13]. Relatively large grains in the surface and middle regions had the <111>-<112> and <100>//AD orientations, respectively, as shown in Figures 6 and 7 [13]. The size spread of grains in the middle region is wider than that in the surface region [13]. The center region shows elongated grains, indicating that it is not fully recrystallized [13].

The texture distribution of the copper wire drawn by 90% and annealed for times ranging from 30 s to 1 h at 700°C showed that, for the wire annealed for 30 s, the <112>//AD component was

distinct in the center region, although it becomes slightly weaker than the <100>//AD component, while the major <100> + minor <111>//AD texture evolved in the middle region and the major <111> + minor <100>//AD texture in the surface region [13]. The intensity of the <100>// AD orientation was strongest in the middle region. For the wire annealed for 1 h, the major component of the texture of the surface region could be approximated by the {110}<001> orientation (<110>//RD and <001>//AD, where RD stands for the radial direction). The texture of the wire grown abnormally after annealing at 700°C for 1 h could be approximated by a <111>-<112>//AD with a weak <112>//AD component.

As mentioned in Section 2.1, two texture transitions occurred in the 90% drawn copper wires during annealing at 700°C, as shown in Figure 4 [13]. One is the transition from the <111>//AD deformation texture to the <100>//AD Rex texture in the early stage of annealing and the other is the transition from the <100>//AD Rex texture to the <111>-<112>//AD abnormal grain growth texture in the later stage of annealing, neglecting minor components [13]. The later stage transition is now discussed. Unlike the early stage transition, the second stage transition is likely to occur as a result of grain growth driven by grain boundary energy [13]. The microstructural change of the drawn copper wires during annealing at 700°C indicates that the increase of the <111>-<112>//AD components and the decrease of the <100>//AD component are caused by abnormal grain growth (Figure 5) [13]. It can be seen that abnormal grain growth starts to occur just below the wire surface, followed by growth into the center [13]. This result indicates that the surface region is in better position to undergo abnormal grain growth. The abnormal grain growth consistently took place in annealing atmospheres of air, argon, hydrogen, and vacuum ($1x10^{-4}$ Torr) [13]. Therefore, the abnormal grain growth is not related to the wire surface. Typically abnormal grain growth in bulk materials can take place if one or more of the following conditions are satisfied: 1) the presence of dispersion of coarsening pinning particles, 2) a wide spread in grain sizes, and 3) a strong texture [12]. Any second phase particles was not seen in TEM of the annealed specimen. Therefore, the effect of dispersions can be neglected [13]. The grain size distribution along the radial direction of the longitudinal section of the wire drawn and annealed for 1 h at 700°C did not show substantial abnormal grain growth [13]. The average grain sizes and the size distributions of grains smaller than 2 $\bar{R}$, where $\bar{R}$ denotes the average grain size, were similar in all regions [13]. Relatively large grains in the surface, middle, and center regions had the <111>-<112>, <100>, and <111>-<112>// AD orientations, respectively [13]. The size spread of grains in the middle region was the widest, while in the surface region it is the narrowest [13]. According to Hillert's statistical model for grain growth in the steady state, the grain growth rate is given by [5]

$$\frac{dR}{dt} = A\left(\frac{1}{\bar{R}} - \frac{1}{R}\right) \tag{14}$$

where A is a factor depending on mobility, grain boundary energy, and grain shape. The model indicates that a grain having $R < \bar{R}$ will shrink and one with $R > \bar{R}$ will grow; if a grain larger than 2 $\bar{R}$ existed, then abnormal grain growth would occur [13]. Also, in terms of the local size distribution, the larger a grain is in comparison with the neighboring grains, the faster the

grain grows [13]. If the size effect controls the texture, the <100>//AD oriented grains will be in better position to grow, making abnormal grain growth occur in the middle region [13]. This prediction is at variance with the experimental results. Therefore, the grain size effect does not seem to be related to the abnormal grain growth accompanying the development of the <111>-<112>//AD texture in the surface region [13]. In order to investigate the effect of texture on abnormal grain growth, the orientations of abnormally growing grains were measured and compared with the local texture of normally growing grains in the near-surface region [13].

Figure 6 shows the texture distribution of the drawn copper wire annealed for 1 h at 700°C. In the annealing condition, extensive abnormal grain growth is not seen (Figure 5 b). The major component of the texture of the surface region can be approximated by <001>//AD; <110>//RD (Figure 6). Special boundaries originating from the evolution of texture is known to play a substantial role in grain growth [8,14-21]. In order to reduce the energy stored in the material in the form of grain boundaries, grain boundaries migrate and the migration of grain boundaries plays an important role in the microstructure and texture evolutions during normal or abnormal grain growth [13]. It has also been reported that the motion of grain boundaries is controlled by the grain boundary mobility at relatively high temperatures, whereas the grain boundary migration is determined by the triple junction mobility at low temperatures [14]. The grain boundary migration depends on the structure and energy of grain boundaries. The migration velocity, v, is generally assumed to be directly proportional to the driving force, P, originated from the grain boundary energy and the mobility, M [15]. That is,

$$v = MP \tag{15}$$

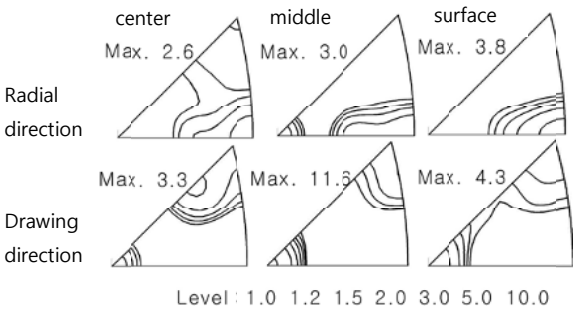

Figure 6. Textures in center, middle, and surface regions of 90% drawn copper wire after annealing for 1 h at 700°C [16].

The grain boundary energy and mobility depend on the grain boundary structure, which can be described by misorientation, causing the growth rate anisotropy. The formation of the special boundaries around a specific grain in a textured matrix has a great effect on the selective grain growth [16-18]. The grain boundary energy and mobility also depend on the segregation of impurity atoms [19]. The grain boundary energy may vary by 20% or less, but the mobility

may vary by orders of magnitude [20]. It has been also known that for fcc metals tilt boundaries migrate much faster than the twist boundaries [14]. As mentioned above, the normally growing grains in the surface region of the wire had a fiber texture consisting of major <100>//AD and minor <111>//AD components and the grain boundaries of the wire can be approximated by tilt boundaries of <100> and <111> rotation axes [13]. Grain boundary mobility data for copper are not available, but the data of the misorientation dependence of the tilt grain boundary mobility in aluminum is shown in Figure 2, which illustrates that the average mobility of <111> tilt boundary is far higher than that of <100> boundary above 400°C. If the grain boundary characteristics of copper are similar to those of aluminum, then the mobility of <111> tilt boundaries of copper will be much higher than that of <100> tilt boundaries, and so neighboring the <111>//AD grains will grow faster than neighboring <100>//AD grains, resulting in larger <111>//AD grains, which in turn will grow at the expense of <100>//AD grains because they now have a size advantage [13].

Taking into account that no abnormal grain growth occurred in the middle region whose texture also consists of major <100>//AD and minor <111>//AD components having only a different intensity ratio compared to the surface region [13], it is clear that a statistical condition of the neighboring events of <111>//AD or <100>//AD grains is needed for the abnormal grain growth of <111>//AD grains. The grain size distribution should also be taken into account. In the surface region, the <111>//AD grains larger than the <100>//AD grains will have greater size advantage due to the neighboring event, while in the middle region the <100>//AD grains larger than the <111>//AD grains might be attributed to hindering the growth of <111>//AD grains [13]. The development of the <111>//AD texture at the expense of <100>//AD texture by abnormal grain growth was also observed in drawn silver wire (Section 2.1).

Note that the development of the {110}<001> texture is extensive in the surface region during annealing at 700°C [13]. In the early stage of annealing at 700°C, the texture is characterized by a fiber texture, which means the orientations of grains are distributed with equal probability around the wire axis, resulting in weak texture along the radial direction [13]. Further annealing at 700°C leads to the evolution of the textures along the radial direction, and the increase in the intensity is more noticeable in the surface region than elsewhere [13]. The further annealing also leads to the increase in the intensity of the <100>//AD texture in the surface region, compared with that of primarily recrystallized wire. Consequently, the {110}<001> texture developed in the surface region [13]. It is interesting to note that in the surface region the texture resulted from grain growth is identical to the texture formed by dynamic recrystallization during drawing. Even so, the reason of the texture recurrence is ambiguous [13].

Figure 7 shows the orientations of abnormally grown grains located in the surface region of 90% drawn copper wire after annealing for 1 h at 700°C. The orientations of abnormally grown grains are approximated by {110}<112>, and the texture of the neighboring grains by {110}<001> in the surface region [13]. The measurements of the orientations of an abnormally grown grain and of its neighboring grains along both the radial and drawing directions can determine the crystallographic characteristics of the grain boundaries for these two kinds of grains [13]. There has been no prior research that has reported the crystallographic relationship of the special boundaries for abnormal grain growth in wire materials because the texture along the radial

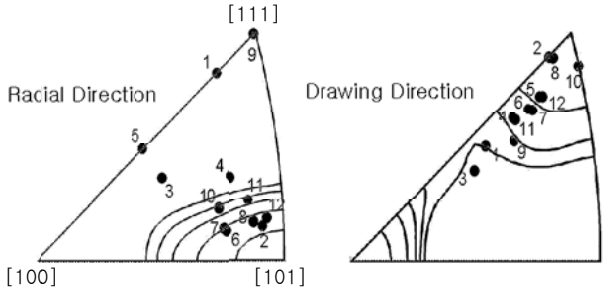

Figure 7. Textures of the surface region (contours) and orientations (black symbols) of large grains (50-250 μm) in the surface region of 90% drawn copper wire after annealing at 700°C for 1 h [13].

direction has not been considered [13]. As can be seen in Figure 8, the {110}<112> orientation of abnormally grown grains and the {110}<001> orientation of neighboring grains, for example, (1-1 0)[112] and (1-1 0)[001], can form a 35.3°<110> tilt grain boundary [13]. The misorientation dependence of the tilt grain boundary mobility in aluminum in Figure 2 shows that 35°<110> tilt boundary leads to a high mobility at high temperatures [13]. These indicate that the grain boundaries formed by the {110}<112> and {110}<001> grains in the surface region of the copper wire have higher migration rates than other boundaries, resulting in the abnormal grain growth [13]. Twinning did not seem to play a role in the progress of the abnormal grain growth in the copper wire from the observation that coherent twin boundaries did not form boundaries between the abnormally grown grains and the matrix, and even isolated twins were found inside the abnormally grown grains [13].

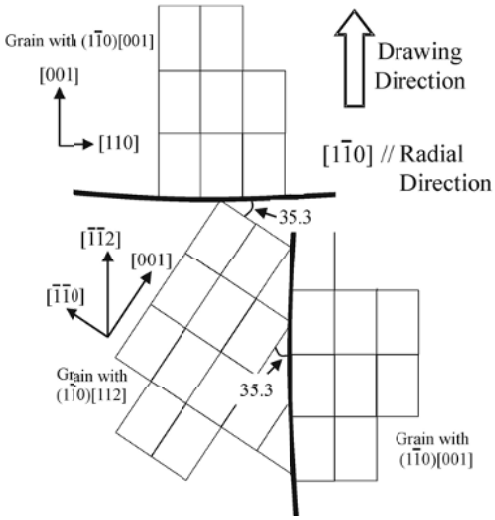

Figure 8. The 35.3°<110> tilt boundaries made by the {110}<112> and {110}<001> oriented grains in fcc lattice [13].

3. Abnormal grain growth textures in nanocrystalline deposits

3.1. Freestanding nanocrystalline Ni and Fe-Ni electrodeposits

The texture change during annealing of a Fe-Ni electrodeposit of several nanometers in grain size was reported by Czerwinski et al. [21]. The Fe-Ni electrodeposit had initially a duplex texture of <100>//ND and <111>//ND with the pole density of the former being a little higher than that of the latter, where ND indicates the deposit-surface normal direction. As annealing proceeded, the pole density of <111>//ND rapidly increased as shown in Figure 9. Similar results were obtained by Park et al. [22,23]. They obtained 30-μm-thick Ni and 20-μm-thick Ni-20 % Fe electrodeposits from Watts-type solutions. The grain size of the Ni electrodeposit was estimated to be 15 to 25 nm, and the grain size of the Ni-20 % Fe deposit was estimated to be 10 to 20 nm. The textures of the both deposits were approximated by the major <100>//ND + minor <111>//ND, which changed to the major <111>//ND + minor <100>//ND after annealing as shown in Figures 10 and 11. Figure 10 shows {111} and {100} pole figures of the nanocrystalline Ni electrodeposit before and after annealing at 300°C for 5 min. Figure 11 shows {111} and {100} pole figures of the nanocrystalline Ni-20% Fe electrodeposit before and after annealing at 400°C for 30min. The pole figures were measured with an X-ray pole figure device (Target: CoK_{α}). These results indicate that the deposition texture characterized by major <100>//ND and minor <111>//ND components changes to the texture consisting of major <111>//ND and minor <100>//ND components after annealing. It should be noted that all the deposits are free standing foils separated from the substrates and the grain sizes of the foils are in the order of 10 nm. Such small grains have little dislocations and so the dislocation effect on the texture transition can be excluded. The thicknesses of the foils are over 1000 times larger than the grain size. Therefore, the surface energy effect can be neglected. The most important factors dominating the texture change are the grain boundary energy and mobility. In this case, the texture transition is similar to that in abnormal grain growth textures in drawn fcc metals (Section 2). The explanation in Section 2 can apply to the present case [24,25]. Park et al. [22,23] also found that the lattice constants of the <100>//ND oriented grains in the as-deposited Ni and Ni-Fe alloy were larger than those of the <111>//ND oriented grains. Lee [26] suggested one explanation of the lattice constant problem based on differences in concentration between the <100>//ND and <111>//ND grains. It should be mentioned that all the data were obtained from freestanding samples. Therefore, any stress effect due to the substrate is excluded. Organic additives in electroplating baths are believed to be partly adsorbed on the deposit, some of which are likely to decompose under high electric fields during electrolysis [26]. Whatever the adsorbates may be, they can hinder growth of electrocrystallites, which in turn results in nanocrystalline deposits [26]. Figure 12 (a) shows that the (111) and (200) interplanar spacings after annealing are on the extrapolated lines of the data at 400°C and 500°C, respectively. The extrapolated lines are parallel to each other [26]. The thermal expansion coefficient obtained from the lines is 15.46×10^{-6} K^{-1}, which is a little higher than the reported value (12.3×10^{-6} K^{-1}) [27,28].

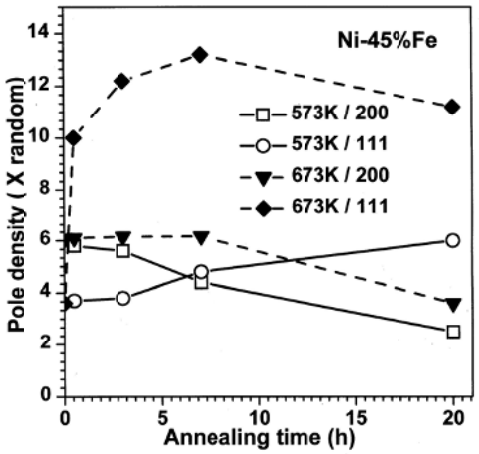

Figure 9. Change in texture of nanocrystalline Fe-Ni electrodeposit during annealing at 573 and 673 K [21].

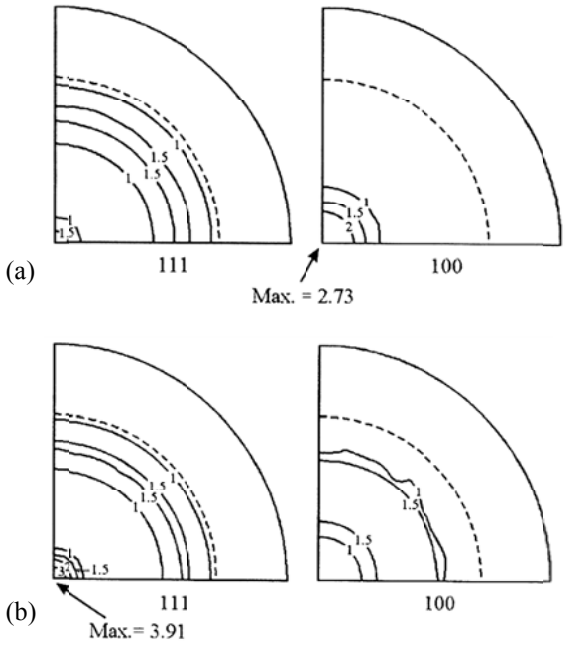

Figure 10. {111} and {100} pole figures of Ni electrodeposit: (a) before and (b) after annealing for 5 min at 300°C [23].

http://dx.doi.org/10.5772/59724

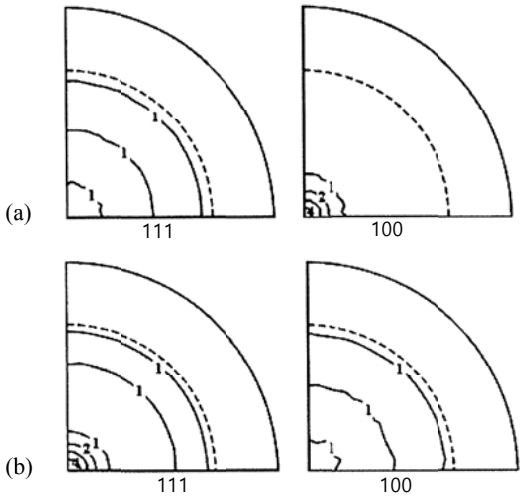

Figure 11. {111} and {200} pole figures of 20%Fe-Ni electrodeposit: (a) before and (b) after annealing for 30 min at 400°C [22].

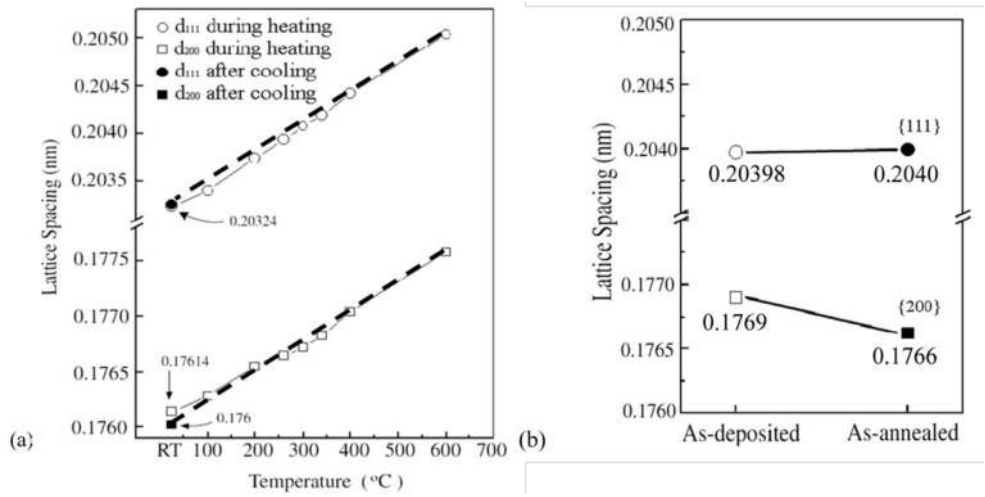

Figure 12. (200) interplanar spacing of <100>//ND grains and (111) interplanar spacing of <111>//ND grains in (a) Ni electrodeposit as a function of temperature and in (b) Fe-80%Ni electrodeposit before and after annealing for 30 min at 400°C [23].

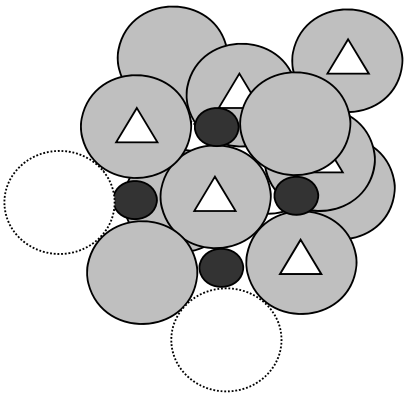

Figure 13. Fcc unit cell showing largest interstitial holes (black spheres) on one (100) plane. Plane made of spheres marked with white triangles is (111) plane. Radius of interstitial hole = ($2_{1/2}$ –1) (atom radius) [26].

The fact that the (111) interplanar spacing at room temperature changes very little after annealing, while a decrease in the (200) interplanar spacing at room temperature after annealing implies that adsorption of something increasing the lattice constant on the {100} planes normal to the growth direction of deposits (ND) is preferred to adsorption on the {111} planes normal to ND [26]. The largest interstitial holes in the fcc lattice are located at <1/2 0 0> as shown in Figure 13. Therefore, adsorption on the {100} planes of the <100>//ND grains is expected to be favored than on the {111} planes of the <111>//ND grains [26]. One candidate of products from decomposition of the organic additives can be carbon [26]. If carbon atoms occupy the <1/2 0 0> interstitial holes, the lattice constants increase and the interplanar spacing increases because the interatomic distance of carbon (graphite) is 0.1421 nm (Table 1), which is larger than the diameter of the largest interstitial hole of nickel, ($\sqrt{2}$ –1) D_{Ni} = 0.1032 nm, where D_{Ni} is the interatomic distance of Ni (0.2492 nm) [26]. However, when the deposit undergoes grain growth during annealing, the interstitial atoms in the <100>//ND grains are likely to be ejected to grain boundaries and some of them diffuse to the <111>//ND grains [26]. In this way, the lattice constants of the <100>//ND grains decrease and those of the <111>//ND grains slightly increase. This seems to be the case of the result in Figure 12 (a) [26]. The interatomic distance of fcc Fe at 25°C was calculated to be 0.2579 nm (1+23×10^{-6}(25-916)) = 0.2526 nm (Table 1, Calc.) [26].

Constant	Ni	fcc Fe (911 to 1392°C)	Graphite	Ref.
Atomic weight	58.71	55.85	0.1421 nm	[29]
Mean therm. expans. coeff.	-	23×$10^{-6}$$K^{-1}$(916 to 1388°C)		[30]
Interatomic distance	0.2492 nm	0.2579 nm (916°C)		[29]
		0.2526 nm (25°C)		Calc.

Table 1. Physical constants of Ni, fcc Fe and C

20 % Fe-80 %Ni = 20.8 atomic % Fe-79.2 atomic% Ni
(111) interplanar spacing of Ni = interatomic distance × $(2/3)^{1/2}$ = 0.20347 nm
(200) interplanar spacing of Ni = interatomic distance × $2^{-1/2}$ = 0.1762 nm
(111) interplanar spacing of Fe = interatomic distance × $(2/3)^{1/2}$ = 0.20625 nm
(200) interplanar spacing of Fe = interatomic distance × $2^{-1/2}$ = 0.1786 nm
(111) interplanar spacing of Fe-Ni = 0.20625 nm × 0.208 +0.20347 nm × 0.792 = 0.2040 nm
(200) interplanar spacing of Fe-Ni = 0.1786 nm × 0.208 + 0.1762 nm × 0.792 = 0.1767 nm

Table 2. Lattice spacing at 25°C calculated using data in Table 1 [26]

The (200) and (111) interplanar spacings calculated using the interatomic distance of Ni (0.2492 nm) are 0.1755 nm and 0.2027 nm, respectively [26]. The (200) interplanar spacing of the annealed <100>//ND grains calculated using the synchrotron XRD data (0.176 nm in Figure 12(a)) is 1.0028 times larger than 0.1755 nm [26]. The (111) interplanar spacing of the annealed <111>//ND grains calculated using the synchrotron XRD data (0.20324 nm in Figure 12 (a)) is 1.0027 times larger than 0.2027 nm [26]. This indicates that the lattice constants of the annealed <100> and <111>//ND grains are almost the same, and are 1.0027 to 1.0028 times larger than those of pure nickel due to some interstitial elements [26].

For the Fe-Ni deposit, Lee [2] evaluated the composition based on the data in Figure 12 (b). For an fcc crystal, the ratio of the (111) interplanar spacing to the (200) interplanar spacing is $2/\sqrt{3}$ (=1.1547) [26]. The ratio of the (111) interplanar spacing in the <111>//ND grains to the (200) interplanar spacing in the <100>//ND grains of the annealed specimen is 1.15496 (=1.000225 times the theoretical value) that is almost the same as the theoretical value, while the ratio of the (111) interplanar spacing in the <111>//ND grains to the (200) interplanar spacing in the <100> grains of the as-deposited specimen is 1.15305 that is 1.00143 times smaller than the theoretical value [26]. This result indicates that the composition of the annealed specimen is homogenized, whereas the lattice constants of the <100>//ND grains in the as-deposited specimen are larger than those in the <111>//ND grains [26]. Assuming that the annealed specimen is completely homogenized, the interplanar spacing has been adjusted so that the ratio of the (111) interplanar spacing to the (200) interplanar spacing in Figure 12 (b) is $2/\sqrt{3}$. The adjusted (111) and (200) interplanar spacings are 0.20399 nm and 1.7666 nm, respectively. From the data in Figure 12 (b) and Table 2, we obtain

$$0.20347X_{Ni} + 0.20625X_{Fe} = 0.20399 \tag{16}$$

$$\text{or } 0.1762X_{Ni} + 0.1786X_{Fe} = 1.7666 \tag{17}$$

$$X_{Ni} + X_{Fe} = 1 \tag{18}$$

where X_{Ni} and X_{Fe} are the atomic fraction of Ni and Fe, respectively. Solving the above equations, we obtain X_{Ni} = 0.81 and X_{Fe} = 0.19. These values are equivalent to 18.2 % Fe and 81.8 % Ni, respectively [26].

As in the Ni electrodeposit, the (111) interplanar spacing of the <111>//ND grains (0.203975 nm) in the as-deposited specimen is slightly smaller than that in the annealed specimen (0.20399 nm), while the (200) interplanar spacing (0.1769 nm) of the <100>//ND grains in the as-deposited specimen is 1.00136 times higher than that in the annealed specimen (0.17666 nm) [26]. The value of 1.00136 is higher than that in the Ni specimen (1.0008), and so, the higher value may not be due only to adsorption of interstitial elements [26]. The interatomic distance of fcc Fe is larger than that of Ni (Table 1), and so the larger lattice spacing in the as-deposited specimen can be attributed to higher concentrations of Fe and interstitial element in the <100>// ND grains than in the <111>//ND grains [26]. The adsorption of interstitial elements is preferred on the <100>//ND grains during electrodeposition, as discussed in the Ni deposit, and hence the interatomic distance of the <100>//ND grains is larger than that of the <111>//ND grains, which in turn gives rise to preferred electrodeposition of Fe on the {100} surfaces of the <100>// ND grains and the higher concentration of Fe in the <100>//ND grains [26]. Since the concentration of interstitial elements in the <111>//ND grains is negligible, the difference in the (111) interplanar spacing between before and after annealing can be attributed to differences in the Fe concentration [26]. Let X_{Ni}^{111} and X_{Fe}^{111} ($X_{Ni}^{111} + X_{Fe}^{111} = 1$) be the atomic fractions of Ni and Fe in the <111>//ND grains in the as-deposited specimen, respectively. It follows from the data in Figure 12 (a) and Table 2 that

$$0.20347X_{Ni}^{111} + 0.20625X_{Fe}^{111} = 0.20398 \tag{19}$$

Solving the above equation, we obtain $X_{Ni}^{111} = 0.8165$ and $X_{Fe}^{111} = 0.1835$, which are higher than the mean atomic fraction of Ni ($X_{Ni} = 0.81$) and lower than the mean atomic fraction of Fe (X_{Fe} =0.19). We calculate the atomic fraction of Fe X_{Fe} in the <100>//ND grains in the as-deposited specimen neglecting interstitial elements. From the following equation

$$0.1786X_{\mathrm{Fe}} + 0.1762\left(1 - X_{\mathrm{Fe}}\right) = 0.1769 \tag{20}$$

we obtain $X_{\mathrm{Fe}} = 0.2917$. This is higher than the mean atomic fraction (0.19) by 0.10 or 53%. This value seems to be too high [26]. If we assume that the effect of interstitial elements is similar to that in the Ni electrodeposit, the value of 0.1769 nm should be reduced as

$$0.1769 \text{ nm} \times 1.76/1.7614 = 0.17676 \text{ nm} \tag{21}$$

If we use this value instead of 0.1769 nm, then 0.1786 X_{Fe} + 0.1762 (1- X_{Fe}) = 0.17676 and we obtain $X_{\mathrm{Fe}} = 0.23$. This is 21% higher than the mean atomic fraction [26].

To conclude, for the nanocrystalline Ni electrodeposits, the <100>//ND grains contains higher carbon atoms located in their interstitial sites than the <111>//ND grains, and for the nanocrystalline Ni-Fe electrodeposit, the concentration of carbon and iron in the <100>//ND grains

is higher than that in the <111>//ND grains [26]. There has been no single report in which the concentration of grains varies with their orientation in a given electrodeposit. Direct experimental verification of the present hypothesis is desirable. The texture changes during annealing in Figures 9 to 11 are in variance with the texture changes in electrodeposits during Rerecrystallization [1,31], in which both the <100>//ND and <111>//ND deposition textures change to the <100>//ND texture after Rex., for fcc metallic deposits. Therefore, we expect that the <100>//ND+<111>//ND duplex deposition texture changes to the <100>//ND texture after annealing. However, the texture changes in Figures 9 to 11 are opposite to our expectation. The annealing texture includes the recrystallization texture and the abnormal grain growth texture [2]. When the deposit is thick enough to neglect the surface energy and/or the interface energy between the deposit and substrate compared with the internal energy due to dislocations, the deposition texture may change after recrystallization [1]. For fcc metals, the <100>, <110>, and <111>//ND deposition textures change to the <100>, <$\sqrt{3}$10>, and <100>//ND textures after recrystallization, respectively, as explained in [1,31]. The evolution of recrystallization textures are well explained by the strain-energy-release maximization (SERM) model [1]. If deposits are obtained at high temperatures or if the grain size of deposits is smaller than the order of 10 nm, the deposits may not have high enough dislocation density to cause recrystallization, and their annealing textures cannot be explained by the SERM model due to dislocations [1]. In this case, the annealing textures will be controlled by stresses that are not caused by dislocations, grain boundary characteristics, and surface and interface energies [2]. When the stresses are dominant, the annealing texture is determined such that the strain energy of deposit is minimal [2]. The texture changes in deposits under the plane-stress, equibiaxial-strain state are discussed in Section 3.2. The plane-stress, equibiaxial-strain state of deposits is caused by their substrates.

Now we are in position to discuss the texture changes in Figs. 9 to 11, the duplex texture of major <100>//ND + minor <111>//ND changing to the texture of major <111>//ND + minor <100>//ND after annealing. The grain sizes of the deposits are in the order of 10 nm. Therefore, the dislocation effect on the texture change can be excluded. The deposits are separated from substrates, and the thickness of them is more than 1000 times larger than the grain size. Therefore, the effects of the interface and surface energies and the strain energy due to different thermal expansion coefficients of deposit and substrate can also be neglected.

It is apparent that the most important factors dominating the texture change are the grain boundary energy and mobility. Lee and Hur [24,25] explained the texture turnover from a (<111>//ND + <100>//ND) to the <111> //ND in fcc metals. The grain boundaries in a material with the duplex fiber texture of <111>//ND + <100>//ND may approximate to tilt boundaries of <111> and <100> //ND grains and boundaries between <111>//ND and <100>//ND grains as shown in Figure 1 [25]. This problem is the same as the texture turnover in Sections 2.1 and 2.2. Therefore, the discussion in Sections 2.1 and 2.2 applies to the present case. In addition to the explanation in Sections 2.1 and 2.2, the <111>//ND grains in the present deposits may be purer than the <100>//ND grains. Therefore, the <111>//ND grains are likely to have higher grain boundary mobilities than the <100>//ND grains and grow at the expense of the <100>//ND grains.

3.2. Electroless Ni-Co-P alloy deposits

Lee and Hur [24, 25] studied texture changes during annealing of the nanocrystalline electroless Ni-Co-P deposits. Electroless deposition is defined as the formation of metal coatings resulting from autocatalytic chemical reduction of metal ions from solution [31]. The metal being deposited is itself catalytic for continuous chemical reduction of the metal ions, and deposition can proceed solely on the desired surface at a rate essentially linear with time. Electrons for electroless deposition are furnished by the reducing agent, unlike electrodeposition which requires a counterelectrode and electrons supplied via a rectifier. Electroless deposition is always associated with the evolution of substantial amounts of hydrogen gas on the depositing surface, whereas hydrogen gas may or may not be evolved during electrodeposition. Otherwise, electroless deposition can be considered analogous to electrodeposition at constant current density; dense deposits are produced and there is no theoretical limit to the coating thickness that can be formed. The electroless Ni-Co-P alloy films were deposited on a preplated 5086 aluminum alloy sheet [24]. The preplating process included cleaning and nitric acid and double zincating treatments [24]. Oxide film formed after alkali cleaning and acid etching was removed by the zincating treatments, to prevent reoxidation and to form catalytic surface. The composition of the electroless deposition bath was 0.07–0.1 mol/L Ni^{2+} ($NiSO_4$), 0–0.03 mol/L Co^{2+}($CoSO_4$), 0.5 mol/L $(NH_4)_2SO_4$, 0.2 mol/L NaH_2PO_2, 0.2 mol/L sodium citrate, and 1 ppm thiourea [24]. The pH of the bath was adjusted to 12 using ammonia solution. The bath temperature was maintained at 90°C [24]. The thickness of deposits ranged from 30 to 40 μm. The micrographs indicated that fine grains were imbedded in amorphous matrix (Figure 14). The amorphous phase is supposed to have a higher phosphorous content than crystalline grains from the well known fact that the electroless Ni-P deposits tend to become amorphous with increasing P content. The electroless Ni-Co-P alloy deposits showed strong (111) and very weak (200) reflection peaks (Figure 15). Their grain size was estimated to be 6 to 7 nm by the Scherrer equation. When annealed at various temperatures for 2 h, the Ni-Co-P deposits showed that the (200) peak intensity increases more rapidly than the (111) intensity with increasing annealing temperature and cobalt content in the deposits.

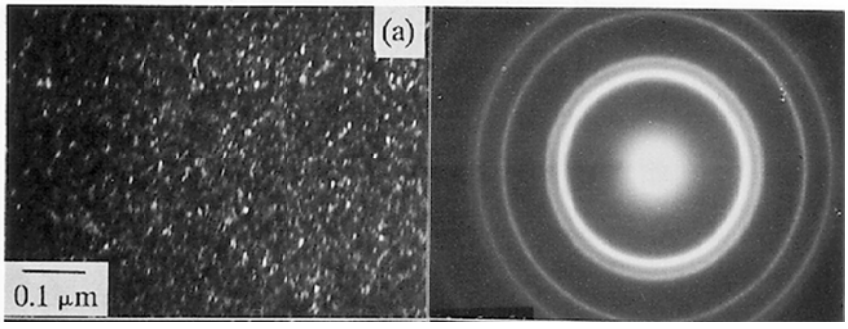

Figure 14. Dark field micrograph and SAD pattern of electroless Ni-2.4Co-7.6P [25].

http://dx.doi.org/10.5772/59724

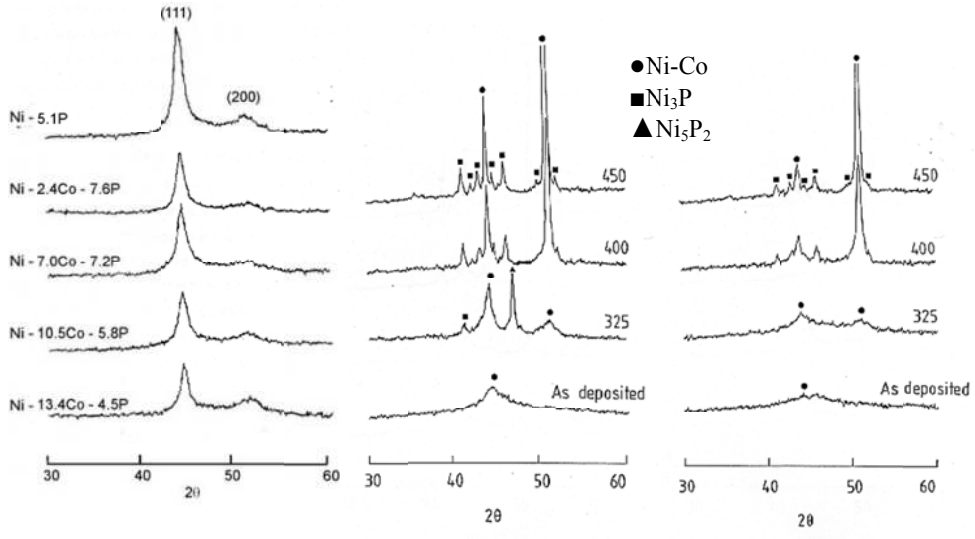

Figure 15. X-ray diffraction patterns of (from left) as-deposited, Ni-2.4Co-7.6P, Ni-10.5Co-5.8P electroless deposits annealed for 2 h. Peak intensities in Ni-2.4Co-7.6P, Ni-10.5Co-5.8P electroless deposits are attenuated [24,25].

At an annealing temperature of 325°C, Ni_5P_2 forms especially in the higher phosphorous deposits, but it disappears and stable Ni_3P appeared at higher temperatures. The similar phenomenon was observed in electroless Ni-Cu-P alloys [31]. The formation of Ni_5P_2 from the annealed Ni-Cu-P deposit is due to a high segregation of P in grain boundary region [25]. When annealed, the high P concentration region was considered to be further increased by extraction of P dissolved in nickel grains, which in turn precipitated the Ni_5P_2 phase. The same explanation can be applicable to the Ni-Co-P deposits [25].

The evolution of the <100>//ND texture in the <111>//ND textured fcc metal films on a substrate during annealing can be attributed to a few sources [32]. The lattice match at the interface between the film and the substrate may lead to the <100>//ND orientation. But the lattice match between the substrate and the nickel alloy deposit has little possibility. When the <111>//ND textured fcc electrodeposits are recrystallized, the <100>//ND texture evolves, as explained in [1,33]. However, this explanation applies to deposits whose dislocation density is high enough to cause recrystallization [33]. Since the grain size of the present deposits is only several nanometers, they are likely to have little dislocation, and so the explanation cannot apply to the present deposits. When grain boundaries control the texture evolution during annealing, the <111>//ND texture is expected to form (Sections 2.1–3.1). The texture change from <111>// ND to <100>//ND may be caused by the fact that the <111>//ND grains have the highest strain energy while the <100>//ND grains the lowest strain energy [34]. The deposit and substrate, which have different thermal expansion coefficients, undergo different volume changes due to a temperature change [24]. In addition, the formation of nickel phosphide could lead to volume changes [24]. These changes can produce strains and in turn stresses in the deposits

during annealing [24]. The experimental results indicated that the texture change was more influenced by the Co concentration than by P, implying that the volume changes due to phosphide formation are not a dominant factor leading to the <100>//ND texture [24]. Therefore, this factor is not considered here.

The strains and stresses due to the different thermal expansion coefficients are calculated. The thermal strain ε_{th} due to the different thermal expansions is calculated by [24]

$$\varepsilon_{th} = \int_{T_0}^{T} (\alpha_s - \alpha_f) dT \tag{22}$$

where T and α are temperature and thermal expansion coefficient, respectively. The subscripts 0, s, and f indicate initial state, substrate, and film, respectively. Setting T = 250 to 450 ℃, T_0 = 90 ℃, $\alpha_s = \alpha_{5086Al}$ = 25.8×10^{-6} K^{-1} [28], $\alpha_f = \alpha_{Ni}$ =13.3×10^{-6} K^{-1} [28], we obtain ε_{th} =(2 *to* 4.5)×10^{-3}. To be more rigorous, the thermal expansion coefficients of fcc Ni-Co solid solutions should be used. The thermal expansion coefficient of cobalt (hcp) is 13.8×10^{-6} K^{-1} [28], which is very close to that of nickel. Therefore, the thermal expansion coefficient of nickel can be a good approximation of the alloys in the absence of experimental values.

A thin deposit on a thick substrate undergoing isotropic thermal expansion is expected to be under a plane stress, equibiaxial strain state. Cubic-symmetry metals undergo isotropic thermal-expansion. Therefore, the Ni-Co-P deposits are likely to be under a plane stress, equibiaxial strain states. The elastic strain energies per unit volume (the strain energy density) of the <100> and <111>//ND films under an equibiaxial strain ε are given by Eqs. 19 and 20, respectively [35,36].

$$w_{(100)} = \varepsilon^2 \left(S_{11} + S_{12} \right)^{-1} \tag{23}$$

$$w_{(111)} = \left[S_{11} + S_{12} + \left(1/6\right)\left(S_{44} - 2S_{11} + 2S_{12} \right) \right]^{-1} \tag{24}$$

Setting S_{11} = 0.00734, S_{44} = 0.00802, S_{12} = -0.00274 GPa^{-1} at room temperature [37], and ε = ε_{th} =(2 *to* 4.5)×10^{-3}, $w_{(100)}$ =0.87 to 4.4 MJ m^{-3}, $w_{(111)}$ =1.55 to 7.86 MJ m^{-3}.

Thus, the <100>//ND grains have lower strain energy than the <111>//ND grains. These values are based on room temperature data [24]. The stresses at experimental temperatures of 250 to 450°C are likely to be lower, but still substantial [24]. To conclude, the evolution of the <100>// ND texture during annealing is caused by preferred growth of <100>//ND grains at the expense of <111>//ND grains under thermal stresses [24].

Electroless Ni-Cu-P deposits show similar grain-size and textures at the initial state [36], but the <111>//ND texture remains relatively stable even after annealing, even though the <100>//

ND texture tends to develop with increasing temperature (Figure 15). This may be due to the fact that the thermal expansion coefficient of copper (19.6×10^{-6} at 700 K [28]) is higher than that of cobalt.

4. Aluminum and copper interconnects

4.1. Textures of Al-1%Cu Interconnects

Field et al. [37,38] deposited 500-nm-thick Al-1%Cu films over Ti and TiN sublayers onto a Si (001) single crystal substrate. The films were patterned into test structures with lines varying from 0.5 to 4 μm in width. A post-patterning anneal at 460°C was then applied to determine its effects on the evolution of texture and grain boundary structure of lines. The resulting structures showed a near-bamboo character for those lines of less than 2.0 μm in width and a polycrystalline structure for the wider lines. The resultant grain size was of the order of 1 μm and varied in proportion to the line width. For an ideal <111>//ND texture, the distribution of crystallographic planes aligned with the grain boundary plane would consist of an arc of uniform intensity extending from the {110} to the {211} in the stereographic unit triangle shown in Figure 16. For wide polycrystalline lines, the measurements of planes along the boundary approximated that of an ideal distribution [2]. For narrow, bamboo-structured lines, the distribution was weighted heavily in favor of the (110) planes aligned with the grain boundary [37,38]. This implies that the line aligns with the <110> direction (Figure 17). The <111>//ND texture strength increased with decreasing line width during the post-patterning anneal [37,38].

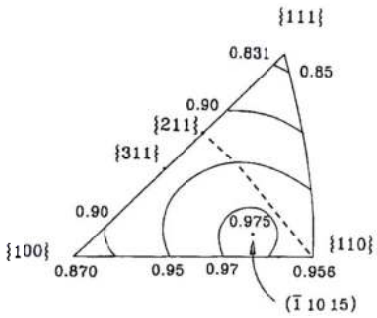

Figure 16. Measured relative surface energy plot for fcc crystal [40]. Dashed line indicates poles of planes normal to {111} planes.

Lee and Lee [2] explained the result in terms of the surface, interface, and strain energies. The surface energy of the (112) plane is the lowest among boundaries normal to the (111) plane (Figure 16) [2]. It is reasonable to assume that the boundaries in the interconnect structure are <111> tilt boundaries [2]. According to the calculated <111> tilt boundary energy (Figure 3c),

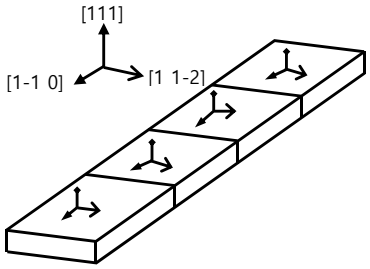

Figure 17. Orientations of grains in bamboo structured line; its texture is approximated by {111}<110> [39].

the (110) boundary does not have the minimum energy, but the boundary energy decreases with decreasing misorientation angle [2]. The line deposits must have had the <111>//ND texture and low dislocation density due to a relatively high deposition temperature, if the usual deposition conditions were used, although the temperature is not given in the papers [38,39]. Therefore, the <111>//ND texture after the post-patterning anneal is believed to result from the grain growth (Section 2 and 3.1). However, the interconnect lines are not guaranteed to have the <111>//ND texture during annealing [2]. Two directional properties should be considered. One is the surface energy and the other is the thermal stress [2]. Among surfaces normal to the (111) surface the {112} planes have the lowest energy (Figure 16). Therefore, when the sidewall surfaces and the surface parallel to the substrate consist of the {112} and {111} planes, respectively, the surface energy of the line has the lowest surface energy. If the surface energy dominates the energy of the line during annealing, the line will be parallel to one of the <110> directions as shown in Figure 17.

4.2. Copper interconnects

The properties of deposited metal films and interconnect structures are sensitive functions of microstructural features. For example, Al-based interconnects (Section 4.1) with a large uniform grain size and a strong <111>//ND texture provide significantly improved reliability. Therefore, an understanding of factors which control microstructural evolution is important for the development and design of reliable, manufacturable interconnect structures, especially in damascene-processed trench interconnects [2].

A structure of damascene trenches is shown in Figure 18. The damascene trenches of various width/space combinations are prepared as grating arrays in a 700-nm-thick FSG layer formed on a Si wafer. A TEOS layer of 300 nm in thickness and subsequently a silicon nitride layer of 55 nm in thickness are vapor-deposited between the FSG and the Si substrate as an etch-stop layer. The trench pattern is made by the lithography on the FSG. TaN of 10 nm in thickness is first sputter-deposited on the FSG as a diffusion barrier and an adhesion layer, followed by sputter-deposition of 150 nm Cu seed layer to serve as cathode for electroplating. The trenches are filled with Cu by electroplating in an acidic sulfate solution with commercial additives. The thickness of Cu deposit over the trench grating is about 700 nm [41].

http://dx.doi.org/10.5772/59724

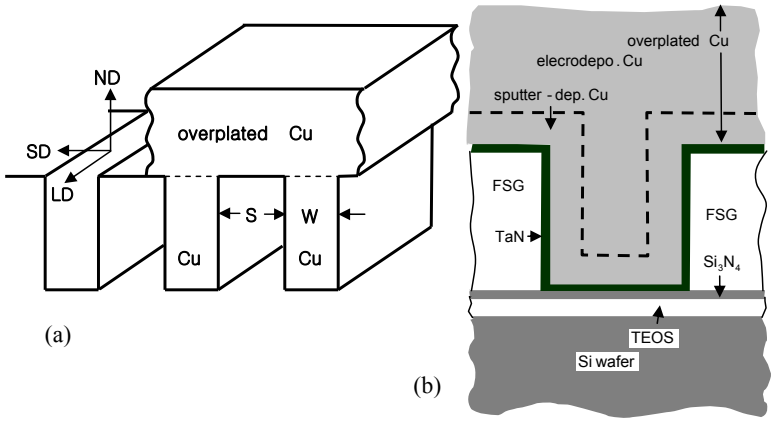

Figure 18. (a) Structure of damascene trenches, where ND, SD, and LD stand for normal direction, sidewall direction, and line direction of trench, respectively. S, W, and Cu indicate space, trench width, and Cu electrodeposit, respectively. (b) Schematic of cross section of electroplated Cu over damascene trench. FSG and TEOS mean fluorinated silicate glass and tetraethylorthosilicate, respectively [41].

Figure 19 shows plan-view electron backscatter diffraction (EBSD) maps of the surface of Cu electrodeposits in 500 nm/500 nm width/space patterned trenches obtained at 2.5 h, 3.5 h, 5.5 h, and 12.5 h at room temperature after Cu electrodeposition. The black area in the EBSD maps indicates the low pattern-quality region. In the low pattern-quality region, the Kikuchi patterns cannot be obtained because the region is too distorted or grains there are too small [41]. The spatial resolution of the EBSD system in the experiment was about 10 nm. Therefore, the grain size in the black area is estimated to be not larger than 15 nm [41]. It took about 30 min to scan from the top line to the bottom line of one specimen to obtain its EBSD map [41]. For the 2.5 h specimen in Figure 19, EBSD scanning started 2.5 h after Cu electrodeposition and finished 3 h after Cu electrodeposition. It can be seen that the black area decreases or the measurable EBSD area increases with increasing time [41]. For the 2.5 h specimen, the measurable EBSD area is seen to increase, even while it is scanned for 30 min. The black vertical lines in the EBSD maps in Figure 19 are related to the blanket area in the trench pattern [41]. The black area including the black line width decreases with increasing time. These results indicate that the grain growth rate is inhomogeneous. The grain growth rate is faster in the pattern area than in the blanket area [41]. According to Lingk and Gross [42], the grain growth initiates at the upper corners of the trench plugs. The number density of corners is higher in the pattern area than in the blanket area. Therefore, the grain growth is faster in the pattern area than in blanket area [41]. The black lines which are related to blanket area are not clearly seen in Figure 19 because of the smaller width of blanket area [41]. To conclude, the initial grain size is not larger than 15 nm and the grain growth occurs even at room temperature. This phenomenon is related to the texture evolution of interconnects, as will be discussed later [41].

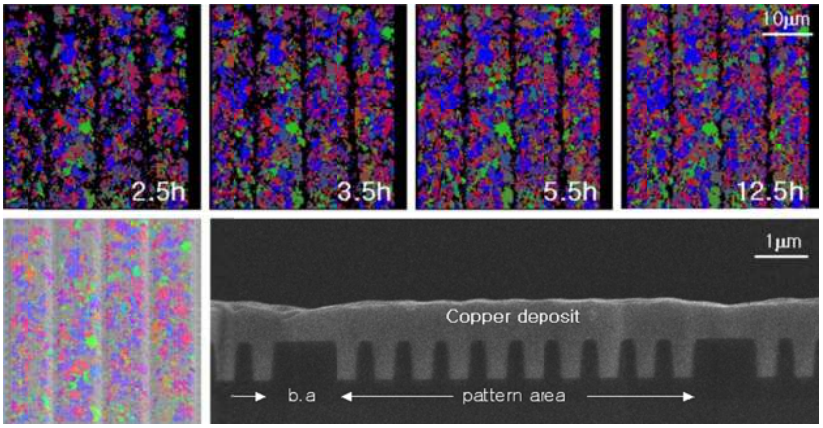

Figure 19. Plan-view EBSD maps of surface of Cu-plated 500 nm/500 nm width/space patterned trenches as a function of time at room temperature following electrodeposition. Black area in EBSD maps is low pattern-quality region. (Left below EBSD maps) Plane-view EBSD map superimposed on corresponding SEM micrograph. (Right below EBSD maps) SEM micrograph of plane normal to trench lines, in which b.a stands for blanket area. Green and blue (light and dark in black-and-white figure) areas in EBSD maps indicate <110>//ND and <111>//ND oriented regions, respectively [41].

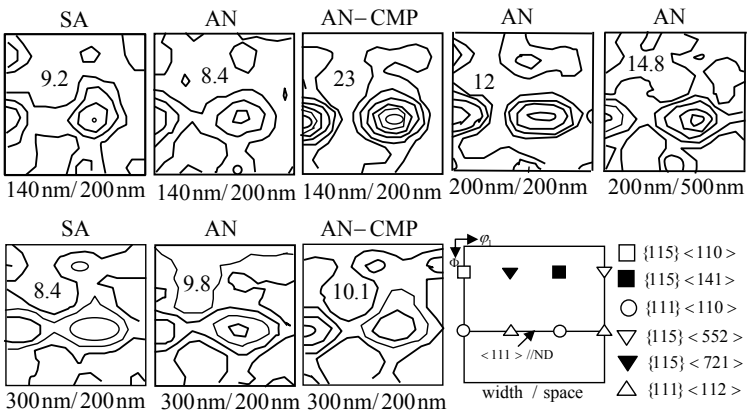

Figure 20. Plan-view ODFs ($\varphi_2 = 45°$) of Cu electrodeposits over various trench/space gratings. SA means self-annealed deposits with over-layer. AN means deposits with over-layer after annealing for 10 min at 200°C. AN-CMP means deposits after annealing for 10 min at 200°C and removing over-layer by CMP. Numerical values in ODFs indicate the maximum orientation density [41].

Figure 20 shows the plan-view ODFs of the surfaces of Cu electrodeposits on various widths/spaces trenches and blanket wafer after self-annealing at room temperature and after annealing for 10 min at 200°C [41]. The textures of all the specimens except the blanket specimen are similar and can be approximated by the {111}<110> texture as a major component and its twin

http://dx.doi.org/10.5772/59724

components {115}<110> and {115}<141> as minor ones [41]. Here {hkl}<uvw> means that {hkl} is the surface plane (<hkl>//ND) and <uvw> is the line direction (LD). The texture of the deposit on blanket wafer is approximated by a <111>//ND texture [41]. Figure 21 shows more annealing texture data on different trench width/space gratings. The self-annealing textures of the 200 nm/200 nm and 240 nm/200 nm width/space patterned trenches can be approximated by a major {111}<110> component and a minor {115}<110> and {115}<141> components, which are twin components of {111}<110>, whereas the texture of the 1000 nm/200 nm width/space specimen is approximated by a major {111}<112> component and a minor {115}<552> component, which is a twin component of {111}<112>. The textures of the 500 nm/200 nm, 2000 nm/200 nm, 500 nm/500 nm, and 500 nm/1000 nm specimens are seen to be mixtures of {111}<110> and {111}<112>, contributions of which vary with specimen.

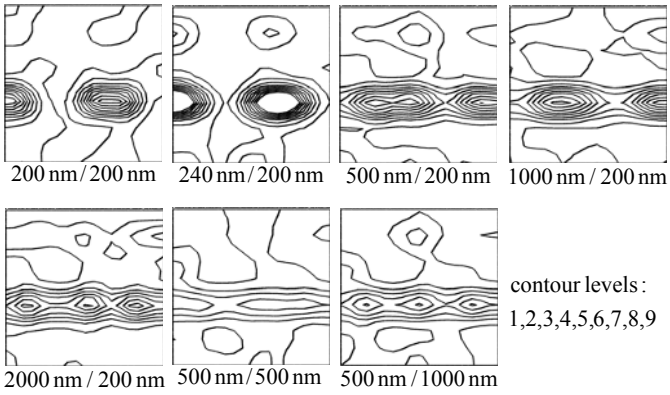

Figure 21. ODF ($\varphi_2 = 45°$) of self-annealed Cu electrodeposits over various trench width/space gratings [43].

Figure 22 shows annealing texture data of Cu damascene interconnects with 0.2-μm space [44]. The textures of the specimens of 0.2 and 0.24 μm in trench width can be approximated by {111}<110> as the major component and its twin components {115}<110> and {115}<141> as minor ones [44]. The textures of the specimens of 0.5 and 1 μm in width can be approximated by {111}<112> with weak <111>//ND [44]. As the width increases, the texture is increasingly of fiber character, with the orientation density decreasing [44]. It is noted that the textures are almost independent of annealing conditions. The {111}<112> texture prevails among the CMP specimens. The 4- and 6-μm-wide specimens show textures approximated by mixtures of diffused {111}<110> and {111}<112> [44]. It is interesting to note that the textures measured over the over-plated layer are similar to those of the CMP-specimens [41]. In order to understand the phenomenon, the structures of the cross sections normal to the trench lines were measured by EBSD [41]. The EBSD maps of the cross sections normal to the line direction (LD) of various trench specimens (Figure 23) show that most grains along with their twins stretch from the bottom of trenches to the surface of over-plated layer. One trench is hardly filled by multiple grains in the normal direction (ND) of trench lines. This is the reason why the plan-view orientations of the copper deposits are almost the same before and after CMP [41].

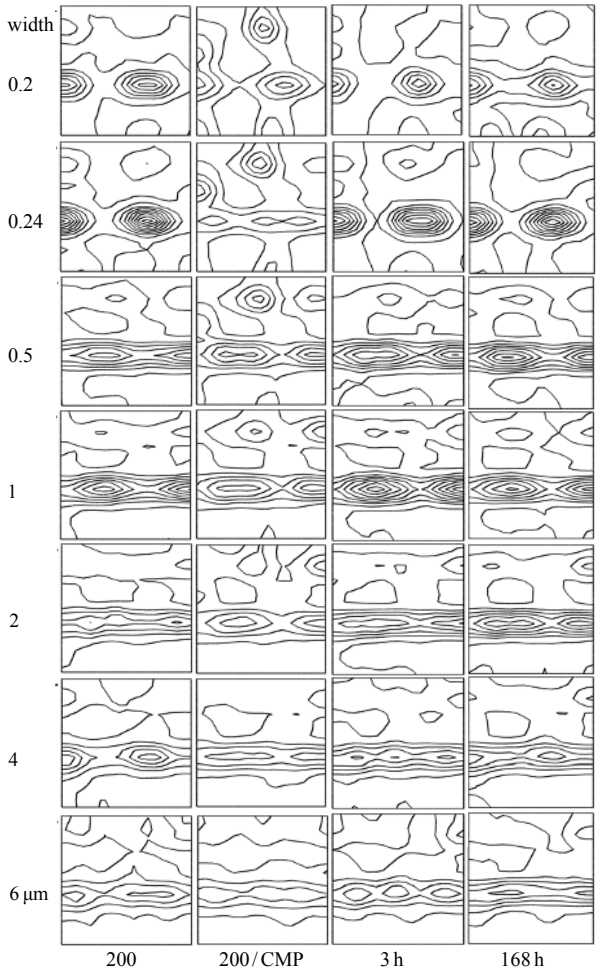

Figure 22. ODF (φ_2 = 45°) of Cu electrodeposits over various trench gratings with 0.2-μm space. Trench width ranges from 0.2 to 6 μm. Specimen (200) annealed for 10 min at 200°C following deposition, (200/CMP) specimen (200) after CMP, (3h) self-annealed for 3 h, (168 h) self-annealed for 168 h [44].

In order to understand the texture results, we must first understand the evolution of the {111}<110> and {111}<112> texture components. The evolution of {111}<110> was first explained by Lee and Lee [43]. Cu deposits electroplated on Cu seed layers have the <111> texture influenced by a strong <111>//ND texture of the seed layers. The seed layers are deposited on the TaN barrier material by sputtering and have a strong <111>//GD texture (GD: the growth direction) [45]. In order to improve filling of Cu deposit in trenches, organic additives are added to the electroplating bath, which hinder growth of electrocrystallites, resulting in fine grain sizes. The initial grain size in the electrodeposits is estimated to be less than 15 nm,

resulting in little dislocation density in the deposit [43]. Therefore, their annealing texture has nothing to do with dislocations. In this case, the annealing texture is controlled by interface energy, grain boundary energy and mobility, surface energy, and strain energy [46,47], and the existing grains that have lower interface, grain boundary, surface, and strain energies and higher grain boundary mobility are in a better position to grow and dominate the annealing texture. This growth texture does not need nucleation for the texture evolution [44]. When a polycrystalline deposit having a fiber texture is annealed under balanced stresses, the annealing texture is likely to of fiber character, whether the annealing texture differs from the deposition texture or not [44]. When the deposit is thick enough to neglect the surface energy and/or the interface energy between the deposit and substrate compared with the internal energy due to stresses, whatever sources they may originate from, the annealing texture will be dominated by the stresses [44]. When the stresses are caused by dislocations, the evolution of annealing texture (recrystallization texture) is well explained by the SERM theory. In the SERM theory [1], the recrystallization texture is determined such that the absolute, maximum stress direction (AMSD) due to dislocation array aligns, at least, with the minimum Young's modulus direction (MYMD) in recrystallized grains, whereby the strain energy release can be maximized. According to the SERM theory, grains whose MYMD is closest to AMSD grow in preference to others. When a polycrystalline material is strained, the strain of each grain can be approximated by the strain of the material, but its strain energy varies because its elastic constants vary with the crystal direction [44]. For simplicity of explanation, we consider the uniaxial tension of a bicrystal consisting of the crystals A and B as shown in Figure 24. Young's moduli E_A and E_B of the crystals A and B differ because of their different orientations. The strain energy densities, w_A and w_B, of the crystals A and B are given by

$$w_A = E_A\varepsilon^2 / 2 \text{ and } w_B = E_B\varepsilon^2 / 2 \tag{25}$$

where ε is the tensile strain. For $E_A > E_B$, the strain energy of A is larger than that of B. A polycrystalline film shown in Figure 25 is considered. Grains whose MYMD is aligned with AMSD have the minimum strain energy. Therefore, the growth of these grains will be preferred. When these grains grow, the strain-energy-release of the film becomes maximized, and the annealing texture is determined by grains whose MYMD is parallel to AMSD. The grain growth rate in a high strain energy region is expected to be higher than in a low strain energy region because the grain growth rate in the high strain energy region reduces the strain energy more rapidly [44].

The strain energy distributions and AMSD in the structures with damascene trenches filled with copper (Figure 18) are considered. The grain size of the copper deposits is of the order of 10 nm as already mentioned [44]. The nanocrystalline deposits have highly strained grains, possibly under tensile stresses because grain boundaries occupy a substantial portion of the volume and are of open structure [44]. Nanocrystalline copper electrodeposits have tensile residual stresses [48-51]. To simulate qualitative distributions of the tensile internal stress field and strain energy in the trenches and their surroundings, Lee et al. [44] have performed a numerical calculation using a finite element code, ABAQUS 6.2. Isoparametric quadratic

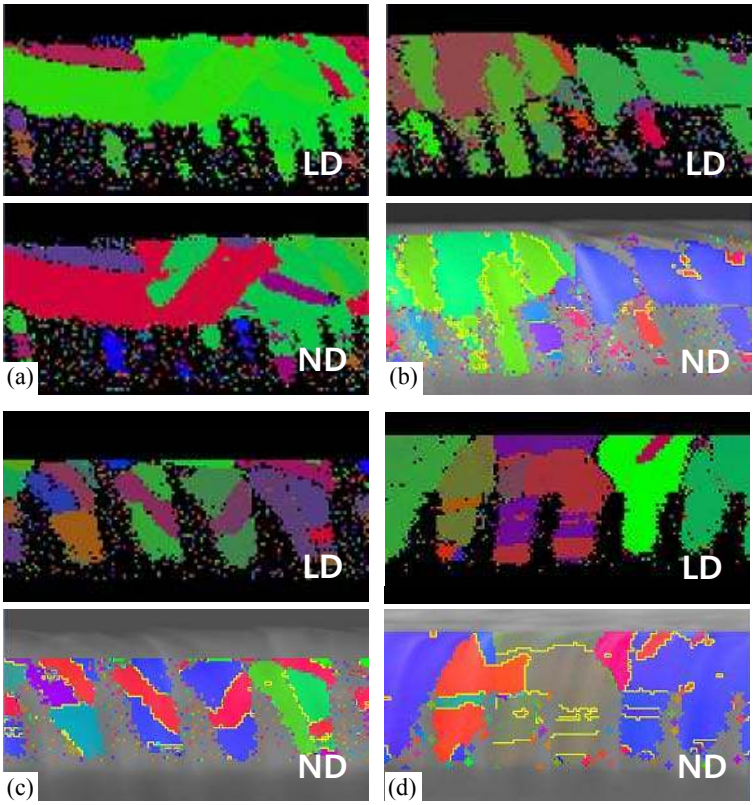

Figure 23. EBSD maps of vertical trench sections. (a) 140 nm/140 nm trench/space grating after self-annealing, (b) 200 nm/200 nm trench/space after self-annealing, (c) 500 nm/500 nm trench/space after self-annealing, (d) 500 nm/500 nm trench/space after annealing for 10 min at 200. Upper and lower figures indicate orientations along line direction and normal direction, respectively. Yellow boundaries indicate twin boundaries [41].

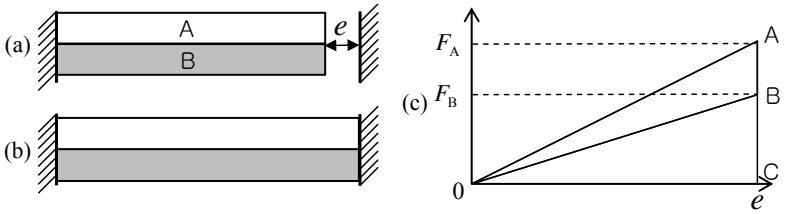

Figure 24. Bicrystal is deformed by displacement e (a) and its both ends are fixed (b). Strain energy of crystals A and B are represented by OAC and OBC (c). Crystals A and B are loaded by forces F_A and F_B, respectively [44].

http://dx.doi.org/10.5772/59724

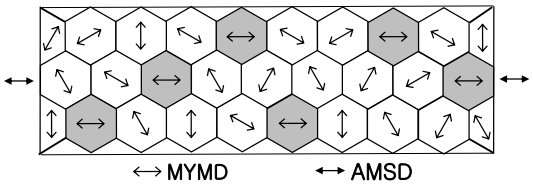

Figure 25. Dark grains whose minimum MYMD is parallel to AMSD grow preferably during annealing and their orientation determines annealing texture [44].

elements were used under plane strain condition, no strain along LD, and the material was assumed to be an isotropic thermo-elastic solid. The cross-sectional structure of a damascene copper deposit including its surrounding materials is shown in the upper right of Figure 26 [44]. The internal stress and strain energy distributions were calculated from the thermal expansion mismatch due to cooling by 40°C. Physical properties of Cu and its surrounding materials are given in Table 1. The strain-energy densities and the maximum principal-stress distributions and directions in the copper deposited in and over three different damascene trenches (a =100 nm and b =200 nm; a =250 nm and b =350 nm; a =400 nm and b = 500 nm) were calculated. One of them is shown in Figure 26. Most of the maximum principal-stress directions in trenches were parallel to the LD of trenches except the high strain-energy regions close to their upper corners [44]. The largest principal-stress direction is in a form of an in-plane stress at the upper corners and is inclined to the deposit surface because of the notch effect of the upper corners [44]. The inclination angle is less than 45° because the thickness of the deposit over the trenches is shorter than the dimension along the surface and less constrained along the ND [44]. It is also noted that the strain energy densities are highest at the upper corners of the trenches. Therefore, the grain growth rate in this region is higher than other regions [44]. This is in agreement with the Lingk and Gross's experimental observation [42] that the grain growth initiates at the upper corners of the trenches [44].

It was observed that the volume fraction of the region, in which the maximum principal-stress directions are parallel to the LD, increases and the strain energy densities at the upper corners increase with increasing width of trenches. The sense of stresses changed, while the strain energy density distributions remain unchanged when the specimens are heated. When the grain growth rate in the high strain-energy region is dominant, the annealing texture is determined such that AMSD at the upper corners of trench is parallel to MYMD of Cu. For the <111>//ND Cu deposit, the MYMD of Cu, the <100> directions, are not on the {111} planes. The directions that are on the {111} planes and at the minimum angle with the <100> directions are the <112> directions as shown in Figure 27. Therefore, grains with the <112> directions have the minimum strain energy among the <111>//ND grains and grow preferably. For Cu deposited in trenches (Figure 18), the <112> directions are parallel to SD. In this case, the <110> directions are parallel to the LD and the {111}<110> oriented grains grow preferably during annealing, resulting in the {111}<110> annealing texture [44]. Similarly, the grain growth rate in the trench, where the AMSD is parallel to LD, is dominant, and the {111}<112> annealing texture is obtained [44].

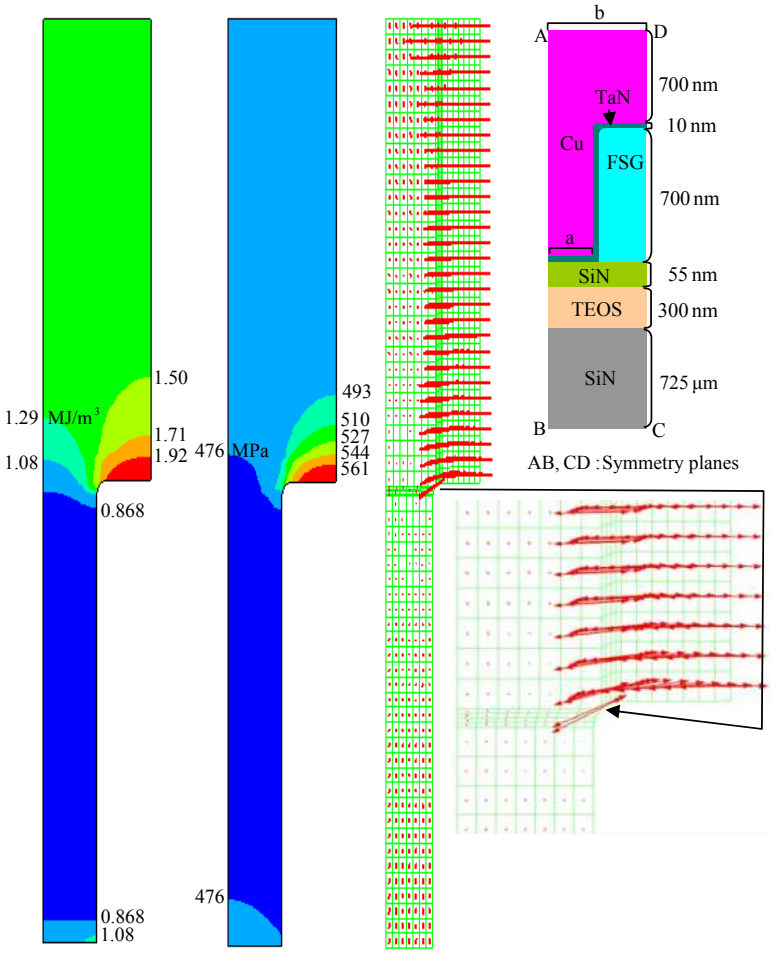

Figure 26. Strain energy density and maximum stress distributions and maximum stress directions (from left) in Cu deposited in and over damascene trench with a = 100 nm and b = 200 nm in Figure 18 [44].

Material	Si(100) Cu [54] TEOS [55] Ta [56] SiN [57] FSG [58]
CTE, ppm/K	2.61 [52] 17.7 1.0 6.5 3.2 0.94
Young's modulus, GPa	131.0 [53] 104.2 59.0 185.7 220.8 71.7
Poisson's ratio	0.278 [53] 0.352 0.16 0.34 0.27 0.16

Table 3. Physical properties of Si(100), Cu, TEOS, Ta, SiN, and FSG.

For the 0.2- and 0.24-μm-wide specimens, the {111}<110> annealing texture was obtained, possibly because the grain growth rate in the high strain-energy region is dominant [44]. As

http://dx.doi.org/10.5772/59724

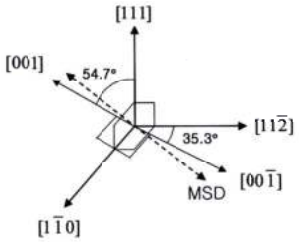

Figure 27. Relationship among [111], [1-10], [11-2], and [001] directions. Maximum stress direction (MSD) and [111], [001], and [11-2] directions are on same plane [2].

the width of trench increases, the grain growth in the trench, where the MSD is parallel to the LD, increasingly prevails, although the strain energy density is low, resulting in the {111}<112> texture [44]. This is supported by the fact that the {111}<112> texture prevails among the CMP specimens (200/CMP in Figure 22). It is noted that when the {111}<112> texture forms, the fiber component is always found, implying that the {111}<110> component cannot be excluded [44]. Up to 2 μm in width, the textures are similar regardless of annealing conditions (10 min at 200°C and 3 h and 168 h at room temperature). The grain growth in the copper deposits is completed in a few hours, resulting in similar textures in the deposits after annealing for 3 h and 168 h at room temperature [44]. Heating at 200°C could develop the sense of stresses opposite to that at room temperature. However, the above discussion still holds. Therefore, the textures of Cu deposits are similar regardless of annealing conditions. As the trench width further increases to 4 and 6 μm, the textures are characterized by mixtures of the {111}<110> and {111}<112> textures or near fiber textures [44]. The relatively high density near φ=15° and φ_1=45° of the CMP specimens seems to be related to the texture of trench walls [44]. This needs further studies.

5. Annealing textures of nanocrystalline copper thin films

Lee et al. [59] studied texture analysis of abnormally grown (abnormal) grains in nanocrystalline Cu films using an automatic orientation- and phase-mapping technique for transmission electron microscopy (TEM). Cu films were deposited by DC sputtering at room temperature onto amorphous SiNx/Si TEM grids with a viewable area of 100x100 μm^2 (Figure 28). They traced the texture evolution of abnormal grains with post-deposition annealing temperature, for which textures of aggregates of grains smaller and larger than specific grain sizes in four types of specimens (as-deposited, annealed for 150 min at 125°C, annealed for 60 min at 300°C, annealed for 60 min at 500°C) were examined. The textures of the aggregate of grains smaller than and larger than a reference grain size are designated as matrix texture and abnormal grain growth (AGG) texture, respectively. The texture of the whole grains, not size-selected grains, is termed overall texture. For the as-deposited film, the overall and matrix textures were dominated by <110>//ND, but <100> //ND grains tended to grow abnormally.

After annealing at high temperatures from 125 to 500°C, the overall and matrix textures were changed to major <112>//ND. The AGG texture was dominated by <112>//ND at 125°C and 300°C. On the other hand, at 500°C, the major AGG texture component was <111>//ND.

In the as-deposited film, <100>//ND grains and a smaller fraction of <111> //ND grains underwent abnormal growth, which can be explained by elastic strain energy minimization and surface energy minimization, respectively. After annealing at 125 and 300°C, AGG developed a strong <112>//ND texture component. After annealing at 500°C, abnormal grains tended to have a major <111>//ND texture component, which is simply explained by surface energy minimization. As annealing temperature increases above 125°C, a strain due to differential thermal expansion would build up, and some grains would undergo plastic deformation before other grains, which is suggested to depend on their Taylor factors. Grains with lower Taylor factors will deform before those with higher factors. Plastically deformed grains are expected to be consumed by grains still remaining in the elastic regime due to the stored strain energy caused by plastic deformation. Among the grains in the elastic regime, grains with the minimum biaxial elastic modulus are likely to grow at the expense of other grains. The hypothesis successfully explained the texture evolution observed after annealing at 125 and 300°C. The attempt also seemed to explain the <112>//ND texture component developed in the Al alloy thin films [69] with little ambiguity.

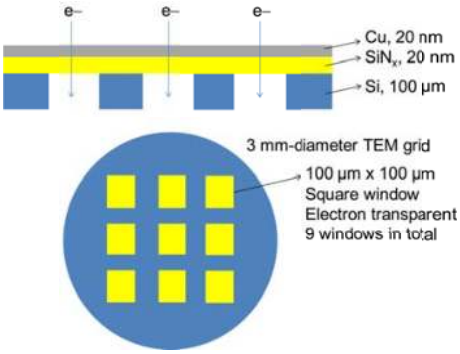

Figure 28. Schematic diagram of Cu films deposited on a grid for in situ TEM (back-etched Si wafer with an amorphous SiN_x membrane [59].

The Cu target purity was 99.999 %. The thickness of the SiN_x membrane which was deposited on 100-μm-thick Si was 20 nm. During deposition, the chamber pressure and the process gas pressure were 2×10^{-7} Torr and 8 mTorr of Ar, respectively. The sputtering power was 2500 W, exhibiting a sputtering rate of ~2 nm/s. The Cu film thickness was determined to be 20 nm. The specimens were subsequently annealed for up to 150 min isothermally at 125°C, and for up to 60 min at 300°C and 500°C in JEM 3011 operating at 300 keV (0.2-nm point-to-point resolution). The heating and cooling rates used were ~5°C/s. The as-deposited film and deposits annealed for 150 min at 125°C, for 60 min at 300°C, and for 60 min at 500°C were

http://dx.doi.org/10.5772/59724

examined for the analysis of texture evolution with post-deposition annealing temperature by using an orientation and phase mapping technique (ASTAR) attached to a field-emission TEM (JEM 2100F) [59]. This technique produced orientation maps similar to the EBSD map obtained in a scanning electron microscope, but exhibits a higher spatial resolution and reasonable acquisition speed for TEM [59]. The setup of the ASTAR system was adjusted to have 2.4 nm in spot size of the electron beam and 4.1 nm in scanning step size.

The raw data obtained from the system was processed by using Orientation Imaging Microscopy™ (OIM™) 6.2 software (EDAX, Draper, U.S.A.) to demonstrate textures of the Cu films in terms of area fraction. The film texture is represented by <*hkl*>//ND, which indicates the <*hkl*> direction of the deposit is parallel to the deposit-surface normal direction (ND). For the matrix and AGG textures, three times the mean grain size was applied as the reference grain size for the as-deposited film and the film annealed at 125°C. As annealing temperature increased further, as will be shown later, the mean grain size did not increase much but larger grains grew fast, leading to the broadened grain size distributions at 300°C and 500°C. Thus a reference of five times the mean grain size was added for the films annealed at these two temperatures.

Orientation data were processed by grain unit. Grains were identified by 5°-misorientation criterion and grains under two pixels were replaced by surrounding pixels to minimize the misindexing influence. For grain size analysis, grains meeting at twin boundaries were considered as one grain [59]. The strength of a texture component [f(g) value] in ODF space cannot reflect the volume fraction of the component directly because there exist overlapped equivalent points of the component in ODF space, which results in the concept of multiplicity. The higher the number of overlapped equivalent points of a texture component in ODF space, the larger its f(g) value [59]. For the quantitative texture analysis of grain growth, they directly calculated area fractions of each major texture component from ASTAR orientation data. Ten-degree criterion is introduced for the determination of each data point as the major texture components because over this criterion, areas for the <112>//ND and <111>//ND components are overlapped.

Figure 29 a shows orientation mapping image, the corresponding grain size distribution and calculated result of area fraction of the as-deposited film. The area fractions correspond to partition fraction in the data captions. Total fraction means a fraction of each component with reference to the whole grains, not size-selected grains. Though not intentionally heated, the film already revealed AGG behavior, as indicated by an arrow in the grain size distribution. For overall deposition texture, the <110>//ND grains occupied the largest area fraction. To extract the AGG texture from overall texture, area fractions of the major components for aggregates of grains smaller than and larger than three times the mean grain size (~35 nm) were calculated (Figure 29 b). The texture of grains smaller than the reference size (matrix texture) shows a major <110>//ND component (Figure 29 b, left). On the other hand, for the AGG texture (Figure 29 b, right), the area fraction of the <110>//ND grains decreases, and those of <100>//ND, and <111>//ND grains greatly increased as compared with the matrix texture, As a result, <100>//ND, <111>//ND, and <110>//ND grains occupied similar fractions, as represented in the bar graph (Figure 29 b).

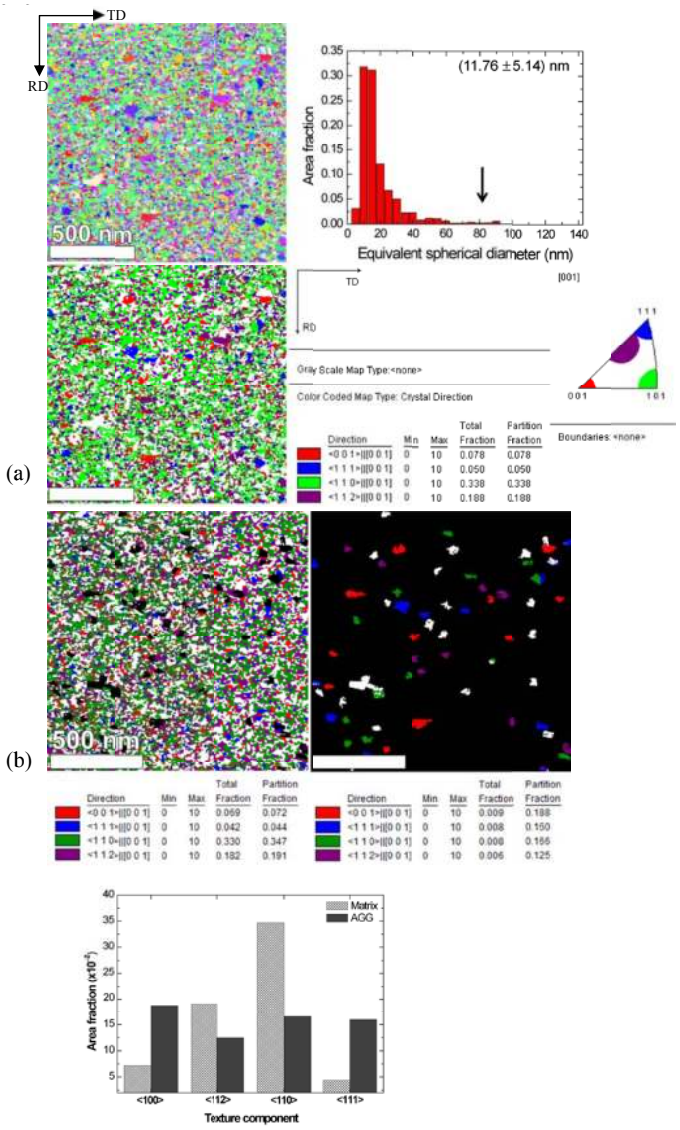

Figure 29. (a) Orientation mapping image and grain size distribution of as-deposited film (upper panel). Average grains size (in diameter) and standard deviation are specified. Area fraction map for the overall data is shown in the bottom left with its color code (bottom right). (b) Area fraction maps of aggregates of grains smaller (left) and larger (right) than reference size of 35.28 nm (3 times mean grain size). Area fractions of texture components in matrix and AGG textures are plotted in bar graph (bottom) [59].

After annealing at 125°C, the overall texture (Figure 30 a, right) was observed to be mainly covered by <112>//ND grains, whereas the area fraction of <110>//ND grains was strongly

http://dx.doi.org/10.5772/59724

decreased from ~0.34 for the as-deposited film to ~0.18. Such tendencies were also reflected on the matrix texture (Figure 30 b, left). Also for the AGG texture, <112>//ND grains occupied the largest area fraction, exhibiting no noticeable difference in area fraction between the matrix and AGG textures. <100>//ND and <111>//ND grains even increased their area fractions in the AGG texture (Figure 30 b, bar graph). For the deposit annealed at 300°C, the overall, matrix and AGG textures were observed to be mainly <112>//ND (Figure 31). However, at variance with the case of the film annealed at 125°C, after annealing at 300°C, the area fraction of <112> grains drastically increased in the AGG texture for both references of three times (Figure 31 b, bar graph) and five times (Figure 31 c, bar graph).

According to a model for development of orientation of vapor deposits [60,61], under the condition of a relatively high vapor concentration adjacent to the deposit induced by high substrate temperatures and evaporation rates, the texture of vapor deposits is dominated by the orientation that places higher surface energy crystal planes (highly stepped surface) normal to the growth direction because, in this regime, grains with highly-stepped surfaces can be in a better position to grow than those with lower-energy surfaces (lowly-stepped surfaces with broad terraces) normal to the growth direction. In contrast, under the condition of a lower vapor concentration adjacent to the deposit induced by relatively low substrate temperatures and evaporation rates, the film texture will be dominated by grains with lower-energy surface normal to the growth direction because the terrace area to be covered by atoms is smaller per unit apparent area. The <110> deposition texture in this study implies that the deposition condition belongs to the regime of a relatively high vapor concentration adjacent to the deposit.

The annealing texture of thin films is determined by energies due to the surface, the film/substrate interface, the extrinsic stress (plane stress-equibiaxial strain or inhomogeneous stress distribution), and intrinsic stress due to dislocations [47]. In this system, the interface energy is unlikely to control the annealing texture because the SiN_x film between the Cu deposit and the Si substrate is amorphous. The initial average grain diameter of the copper deposit was smaller than 20 nm (Figure 29 a). Therefore, the Cu grains are likely to have little dislocation density under no stress. Since the grain size and thickness of the deposit are similar, the surface energy could be important. However, surface energy minimization predicts the <111>//ND texture, and thus cannot explain the <100> and <112> AGG textures (Figures 29-32 and Table 4).

When the layered specimen is heated to 125, 300, and 500°C, the Cu/SiN_x layer can be subjected to a thermal strain, due to the difference in thermal expansion coefficient between the Cu/SiN_x layer and the Si substrate. In this case the Cu/SiN_x layer should be in a plane stress, equibiaxial strain state because the 20-nm-thick Cu/20-nm-thick SiN_x layer is very thin, as compared with the 100-μm-thick Si substrate, and thus its strain is likely controlled by the Si substrate whose thermal expansion is isotropic.

As for the deposit annealed at 125 and 300°C, the deposit annealed at 500°C revealed that the overall and matrix textures were dominated by <112>//ND (Figure 32). For the AGG texture, in the case of a reference of three times (Figure 32 b, bar graph), <112>//ND grains occupied the largest area fraction with that of <111>//ND occupying the second largest area fraction. For a reference of five times, the situation was reversed with <111>//ND grains making up the

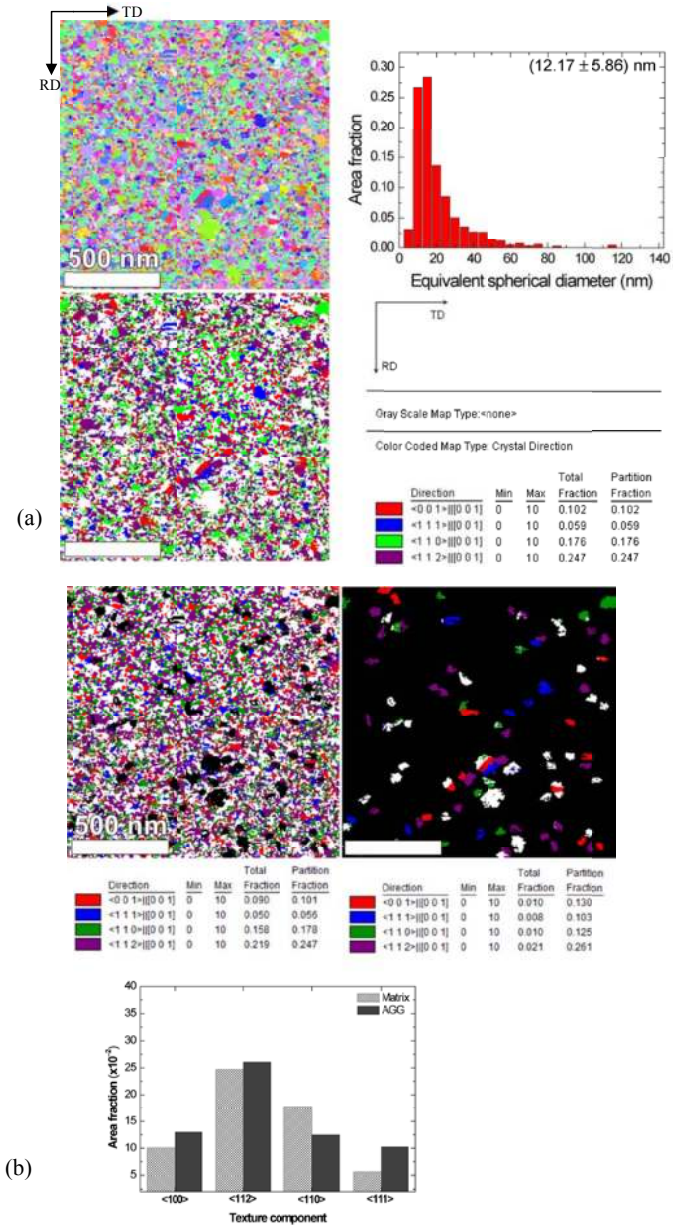

Figure 30. (a) Orientation mapping image, grain size distribution (center), and area fraction map (right) of the deposit annealed at 125°C. (b) Area fraction maps of the aggregates of grains smaller (left) and larger (right) than a reference size of 36.51 nm (3 times the mean grain size) [59].

Temperature	Overall	Matrix	AGG
RT	110	110	100
125 °C	112	112	112
300 °C	112	112	112
500 °C	112	112	111

Table 4. Summary of overall, matrix, and AGG textures for all temperatures examined [59].

largest fraction followed by <112>//ND grains. The summary of overall, matrix and AGG textures for all the temperatures examined is given in Table 4.

Since, for fcc metals, the surface energy increases in order of {111}, {100}, {112}, and {110} (Figure 16), the main <110>//ND component in the overall and matrix deposition textures (Figure 29, Table 4) is not explained by surface energy minimization, but should be considered by growth kinetics. The thermal strain, ε_{th}, due to differential thermal expansion is calculated by

$$\varepsilon_{th} = \int_{T_0}^{T} \left(\alpha_s - \alpha_f \right) dT \tag{26}$$

where T and α are temperature and linear thermal expansion coefficient, respectively; and the subscripts *0*, *s*, and *f* indicate initial state, substrate, and film, respectively. The linear thermal expansion coefficients of Cu, amorphous Si_3N_4 for the SiN_x layer, and Si are 16.5×10^{-6} K^{-1} [http://www.webelements.com], 4.5×10^{-6} K^{-1} [62], and 2.6×10^{-6} K^{-1} [http://www.webelements.com], respectively. During annealing, the Cu layer is likely to undergo an equibiaxial compressive strain of 1.39×10^{-3} [= (16.5–2.6)(125–25) × 10^{-6}] at 125°C, 3.82×10^{-3} [= (16.5–2.6)(300–25) × 10^{-6}] at 300°C, and 6.60×10^{-3} [= (16.5–2.6)(500–25) × 10^{-6}] at 500°C. The strain energy density (the strain energy per unit volume) w of a film under the plane stress, equibiaxial strain (ε) state is given by [35,36]

$$w = \varepsilon^2 M_\varepsilon \tag{27}$$

where M_ε is the biaxial elastic modulus of the film under the plane stress, equibiaxial strain state. The modulus M_ε for a cubic-symmetry material is expressed as Eq. 28 [35,36],

$$M_\varepsilon = \frac{1}{2} \cdot \frac{S'_{11} + S'_{22} - 2S'_{12}}{S'_{11}S'_{22} - \left(S'_{12}\right)^2} \tag{28}$$

where the compliances S'_{11}, S'_{12}, and S'_{22} are given by Eqs. 29, 30, and 31, respectively [35,36].

$$S'_{11} = S_{11} + \left[S_{44} - 2(S_{11} - S_{12}) \right] \left(a_{11}^2 a_{12}^2 + a_{12}^2 a_{13}^2 + a_{13}^2 a_{11}^2 \right) \tag{29}$$

$$S'_{12} = S_{12} - (1/2)\left[S_{44} - 2(S_{11} - S_{12})\right]\left(a_{11}^2 a_{21}^2 + a_{12}^2 a_{22}^2 + a_{13}^2 a_{23}^2\right) \tag{30}$$

$$S'_{22} = S_{11} + \left[S_{44} - 2(S_{11} - S_{12})\right]\left(a_{22}^2 a_{21}^2 + a_{21}^2 a_{23}^2 + a_{23}^2 a_{22}^2\right) \tag{31}$$

For the [*hkl*]//ND crystals, the transformation matrix a_{ij} is expressed as Eq. 32 [35,36].

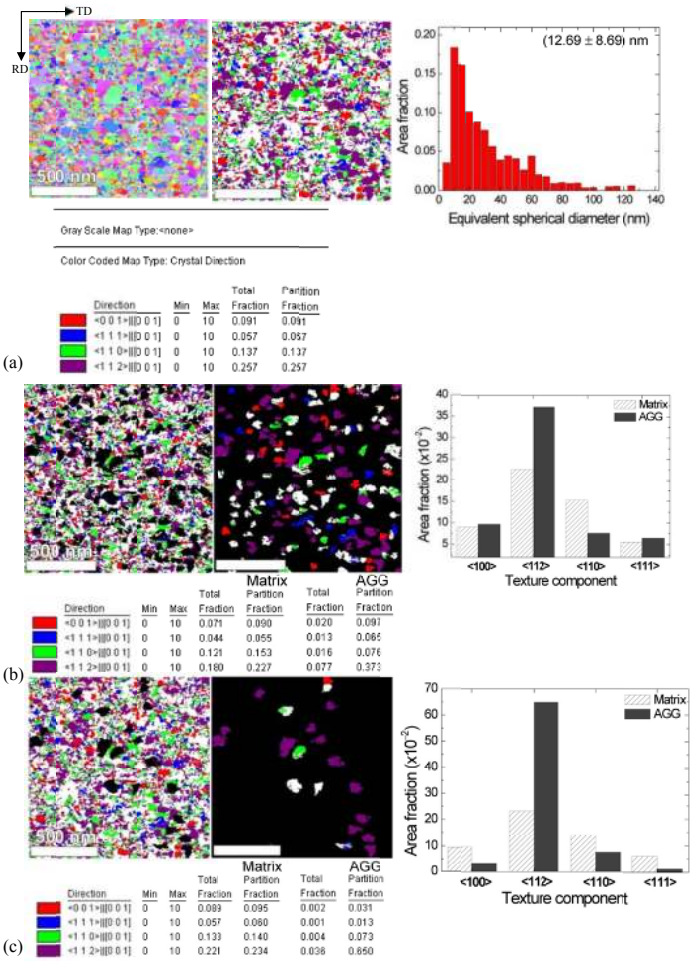

Figure 31. (a) Orientation mapping image, grain size distribution, and area fraction map of deposit annealed at 300°C. (b) Area fraction maps of the aggregates of grains smaller (left) and larger (right) than reference size of 38.07 nm (3 times mean grain size). (c) Area fraction maps of the aggregates of grains smaller (left) and larger (right) than reference size of 63.45 nm (5 times mean grain size) [59].

http://dx.doi.org/10.5772/59724

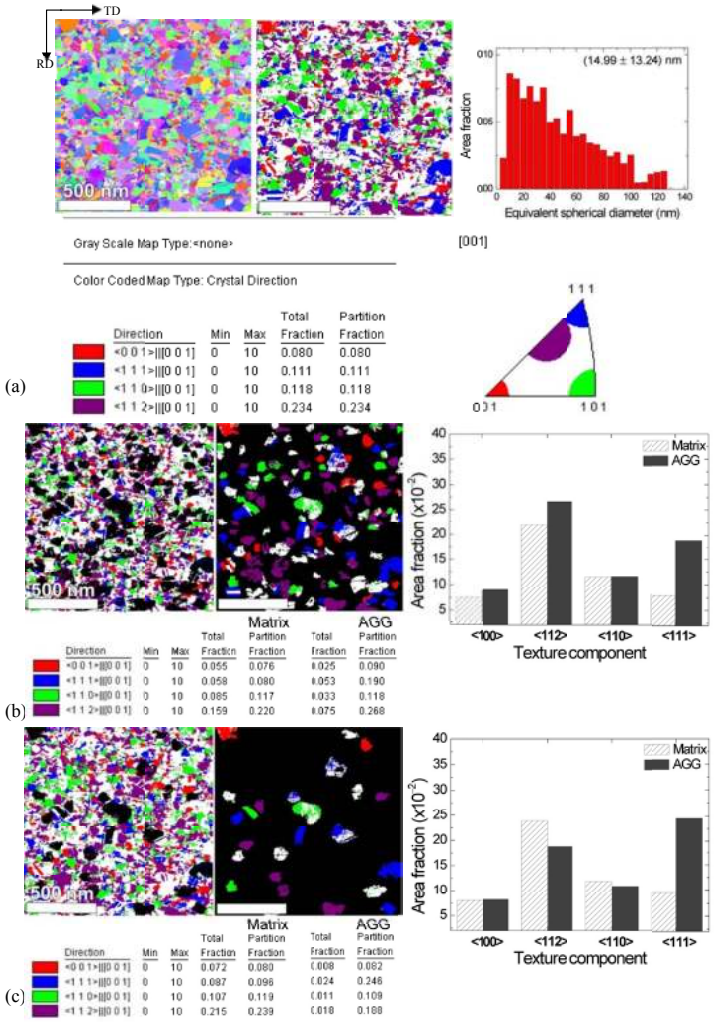

Figure 32. (a) Orientation mapping image (left), grain size distribution (center), and area fraction map (right) of the deposit annealed at 500°C. (b) Area fraction maps of aggregates of grains smaller (left) and larger (right) than reference size of 44.97 nm (3 times mean grain size). (c) Area fraction maps of aggregates of grains smaller (left) and larger (right) than reference of 74.95 nm (5 times mean grain size) [59].

For copper, S_{11} = 0.015635, S_{44} = 0.01368, S_{12} = –006587 GPa^{-1} at 400 K and S_{11} = 0.016718, S_{44} = 0.014472, S_{12} = –0.00691 GPa^{-1} at 550 K [63]. It follows from these data that M_ε of the <100>//ND grain (M_ε <100>) = 110.5 GPa, M_ε <112> = 200 GPa, M_ε <110> = 227 GPa, M_ε <111> = 255.1 GPa at 400 K, and M_ε <100> = 102 GPa, M_ε <112> = 182 Ga, M_ε <110> = 206.2 GPa, M_ε <111> = 230.2 GPa at 550 K. In fact, M_ε <100> and M_ε <111> are the minimum and maximum values, respectively. Note that, as temperature increases, strain energy anisotropy also increases.

$$a_{ij} = \begin{bmatrix} \dfrac{-k}{\sqrt{h^2+k^2}} & \dfrac{h}{\sqrt{h^2+k^2}} & 0 \\ \dfrac{-hl}{\sqrt{h^2+k^2}\sqrt{h^2+k^2+l^2}} & \dfrac{-kl}{\sqrt{h^2+k^2}\sqrt{h^2+k^2+l^2}} & \dfrac{h^2+k^2}{\sqrt{h^2+k^2}\sqrt{h^2+k^2+l^2}} \\ \dfrac{h}{\sqrt{h^2+k^2+l^2}} & \dfrac{k}{\sqrt{h^2+k^2+l^2}} & \dfrac{l}{\sqrt{h^2+k^2+l^2}} \end{bmatrix} \tag{32}$$

As revealed in Figure 29, the as-deposited film already underwent AGG with the <100> and <111> texture components contributing alike. It may imply that during deposition the substrate temperature increased to temperatures above room temperature, thus suggesting that the AGG texture is affected by thermal strain build-up and thus controlled by elastic strain energy minimization. In fact it is well documented that, though the substrate is not intentionally heated, it is warmed by the deposition itself [64]. Considering that <100> grains have the minimum biaxial elastic modulus, the evolution of the AGG texture of <100> for the as-deposited film (Figure 29 b and Table 4) is explained by elastic strain energy minimization. The <111> component in the AGG texture is attributed to surface energy minimization effect, indicating that in the as-deposited film, two representative driving forces (surface energy minimization and strain energy minimization) were competing.

One of the questions to be addressed is why the overall, matrix, and AGG textures after annealing at 125 and 300°C were dominated by the <112> component (Figures 30 to 32 and Table 4). The component seems not related to elastic strain energy minimization because <100> grains have the minimum biaxial elastic modulus. However, as will be discussed below, if we assume that the film system is elastic–plastic and introduce the concept of the Taylor factor, we will be forced to know that the evolution of the <112> component is understood in terms of elastic strain energy minimization. During annealing at 125 and 300°C, the deposit is calculated to undergo the equibiaxial compressive strains of 1.39×10^{-3} at 125°C and $3.82.60\times10^{-3}$ at 300°C, as noted before, and at such high temperatures the critical resolved shear stress on active slip systems is expected to be lowered. Therefore, the deposit may undergo plastic deformation. If every grain undergoes the same strain as the deposit does, operating slip systems and shear strains on the slip systems can differ depending on the orientation of each grain. In order to accomplish an increment of plastic strain, $d\varepsilon_{ij}$, the shear strains, $\sum_k d\gamma^{(k)}$, are needed, where $d\gamma^{(k)}$ is the shear strain on the kth slip system of a crystal. The ratio of the sum of shear strains on active slip systems to the plastic strain increment is often called the Taylor factor (*Tf*) [71], which is expressed as

$$Tf = \sum d\gamma^{(k)} / d\varepsilon_{ij} \tag{33}$$

The *Tf* predicts that the strain energy of grains increases with increasing their *Tf*s. We suppose that the present Cu deposit and its grains undergo the same equibiaxial plastic strain. This

http://dx.doi.org/10.5772/59724

strain state is equivalent to an axisymmetric strain state. Chin and Mammel [65] calculated orientation dependence of *Tf* for axisymmetric deformation for {110}<111> or {111}<110> slip systems. *Tf*s of the <100>//ND, <112>//ND, <110>//ND, and <111>//ND fcc crystals are 2.449, 3.076, 3.674, and 3.674, respectively. *Tf* of the <100>//ND crystal is the minimum and the <110>// ND and <111>//ND crystals have the maximum *Tf*. This means that the <100>//ND grains have the minimum strain energy, and the <110> and <111>//ND grains have the maximum strain energy. Therefore, the <100>//ND grains seems likely to grow at the expense of neighboring grains with higher *Tf*s.

However, all grains in the Cu deposit cannot undergo the same strain as the grain aggregate (deposit) does. The thermal strain increases with increasing annealing temperature. During that course, some grains will undergo plastic deformation before others, and the plastically deformed grains are likely to have higher strain energy due to dislocations generated by plastic deformation than surrounding grains with different orientations, which still remain in the elastic regime. In fact, an increase in *Tf* also means an increase in resistance to deformation and thus *Tf* can be expressed as [72,73]

$$Tf = \sum d\gamma^{(k)} / d\varepsilon_{ij} = \sigma_{ij} / \tau_c \tag{34}$$

where σ_{ij} is the strength and τ_c is the critical shear stress acting on all the active slip system. For instance, grains which are oriented to have infinite *Tf* cannot be plastically deformed. When a polycrystalline aggregate is subjected to a plastic deformation that is not so high enough to make the strengths of grains become similar, low *Tf* grains are likely to deform more than neighboring high *Tf* grains. In this case, low *Tf* grains have higher strain energy than high *Tf* grains, which in turn makes high-*Tf* grains grow at the expense of neighboring low *Tf* grains. These phenomena have been found in annealing textures of Ag [66,67], Cu-bearing bake hardening steel [68], and Al [69].

For convenience's sake, we consider <100>//ND, <112>//ND, <110>//ND, and <111>//ND grains. The <100>//ND grains are likely to begin to be deformed before grains with other orientations because the <100>//ND grain has the lowest *Tf*. For the increased strain (1.39×10^{-3}) at 125°C, we expect that grains with orientations of lower *Tf*s begin to undergo plastic deformation. The evolution of the strong <112>//ND texture after annealing at 125, 300, and 300°C (Figures 30 to 32, Table 4) can be explained by assuming that <100>//ND grains with the lowest *Tf* have been deformed at these temperatures, while grains with the other three orientations remain in the elastic regime. In this case, the <112> grains would grow at the expense of the <110>//ND and <111>//ND grains in the elastic regime. Simultaneously, they are likely to grow by consuming the <100> grains in the plastic regime. As a result, the growth of <112>//ND grains would be favored by elastic strain energy minimization, replacing the textures found in the as-deposited film.

After annealing at 125°C, the area fractions of the <112>//ND component did not vary between the matrix and AGG textures (Figure 30 b), with those of the <100>//ND and <111>//ND grains even increased, whereas the area fraction of the <112>//ND component in the AGG texture

was observed to be much higher than that in the matrix texture at 300°C (Figure 31 b-c). It has been suggested that at 125°C, parts of the <100>//ND grains are still in the elastic regime, contributing to AGG. And at the temperature, strain energy minimization seemed not so completely dominant over surface energy minimization. As mentioned above, strain energy anisotropy is likely to be stronger with increasing temperature further. Thus at 300°C, strain energy minimization would be controlling over surface energy minimization and due to a steady buildup of thermal strain, more <100>//ND grains are expected to belong to the plastic regime. Under such circumstance, when AGG occurred, the <112> grains would make up a dominant area fraction, as shown in Figure 31 b and c. After annealing at 500°C, the <111> component was observed to make up the largest area fraction with the area fraction of the <112>//ND component still comparable (Figure 32 c). The evolution of the <111>//ND component is naturally attributed to surface energy minimization. At such a high temperature, defects inside grains gradually diminish and the surface energy increasingly dominates because the atomic mobility increases with increasing temperature, enabling <111>//ND grains to grow abnormally.

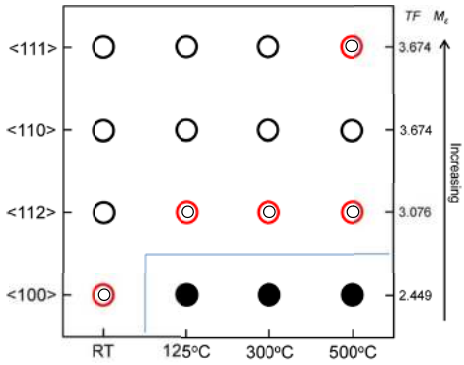

Figure 33. Schematic diagram showing that nanocrystalline grains in film system under plane stress, equibiaxial strain state undergo elastic–plastic transformation with increasing temperature, transition which is closely associated with *Tf*. Open circles indicate grain orientations in elastic regime, while closed ones are in plastic regime. AGG texture is suggested to be dominated by grains with lowest biaxial elastic modulus (M_ϵ) in elastic regime at each temperature, as indicated by the double circles. An exception seems to occur at 500°C, where surface energy minimization becomes dominant, leading to major <111> texture component [59].

Taken together, the evolution of the <100>//ND component during AGG for the as-deposited film is purely explained by elastic strain energy minimization. The <111> component in the AGG textures for the as-deposited film and the film annealed at 500°C is explained by surface energy minimization. The development of the <112> texture for the deposits annealed at 125, 300, and 500°C is made clear by assuming that <100>//ND grains were plastically deformed at these temperatures. Out of grains which have higher *Tf*s and thus are still in the elastic regime, those with the lowest biaxial elastic modulus (i.e., <112>//ND) would grow at the expense of the surrounding grains. This model can apply to the development of <112>//ND during AGG in the <111>//ND matrix Al alloy thin films reported by Longworth and Thompson [70]. These results are summarized in Figure 33.

http://dx.doi.org/10.5772/59724

This study [59] opens a way to the development of a comprehensive mechanism for the AGG texture evolution in thin films taking two factors into consideration: strain energy minimization and *Tfs*. If all grains belong to the elastic regime, the AGG texture is simply determined by elastic strain energy minimization, which explains the development of the AGG texture of <100>//ND found in the as-deposit deposited film. As a thermal strain builds up with increasing annealing temperature above room temperature, grains with lower *Tfs* in thin films will undergo plastic deformation before other grains with higher *Tf*s. In this case, grains undergoing plastic deformation would be consumed by grains still remaining in the elastic regime. Among grains in the elastic regime, grains with the minimum biaxial elastic modulus will grow at the expense of others. As a result, grains with the minimum elastic biaxial modulus out of grains in the elastic regime grow abnormally. The hypothesis well clarifies the evolution of <112> as abnormal grains during annealing at 125 and 300°C.

6. Conclusion

Silver and copper wires subjected to heavy cold-drawing evolve the <111>//AD texture, where AD stands for the axial direction. When recrystallized, the <111>//AD drawing texture turns to the recrystallization texture composed of major <100>//AD and minor <111>//AD. As annealing time prolonged, the <111>//AD component increased, while the <100> component decreases, accompanied by abnormal grain growth. The texture change during abnormal grain growth must be related to grain boundary mobility because the dislocation density drastically decreases during the primary recrystallization and the internal energy of the system is dominated by the grain boundary energy.

The textures (~ major <100>//ND + minor <111>//ND) of free standing nanocrystalline Ni and Fe-Ni alloy electrodeposits of 20 to 30 μm in thickness and in the order of 10 nm in grain size change to the major <111> + minor <100>//ND texture after annealing, where ND indicates the deposit-surface normal direction. The most important factor dominating the texture change is the grain boundary mobility. The texture transition mechanism is similar to that in abnormal grain growth textures in drawn silver and copper wires. Another factor is the <111>//ND grains being purer than the <100>//ND grains.

The structure of electroless Ni-Co-P alloy deposits of 30 to 40 μm in thickness on a 5086 aluminum alloy sheet is characterized by 6- to 7-nm-sized crystallites imbedded in amorphous matrix. The (111) peak intensities of the deposits are much higher than the (200) intensities. When annealed for 2 h, the (200) peak intensities of the deposits increase more rapidly than the (111) intensity with increasing annealing temperature and cobalt content in the deposits [24]. At an annealing temperature of 325°C, Ni_5P_2 forms especially in the higher phosphorous deposits, but it disappears and stable Ni_3P appeared at higher temperatures [24]. The evolution of the <100>//ND texture in fcc metal films with the <111>//ND texture on a substrate during annealing is due to the fact that the <100>//ND grains have lower thermal strain energy than the <111>//ND grains.

When Al interconnects made by patterning of 500-nm-thick Al-1%Cu films of 500 nm deposited over Ti and TiN sublayers onto a Si (001) are annealed at 460°C, a near-bamboo character is obtained for those lines having widths less than 2.0 μm and a polycrystalline structure was obtained for the wider lines. The resultant grain size is of the order of 1 μm and varies in proportion to the line width. For narrow, bamboo-structured lines align with the <110> direction. The <111>//ND texture strength increased with decreasing line width during annealing. The result is explained by the surface energy minimization of the system.

The initial size of Cu grains in Cu interconnects of 700 nm in thickness made by electroplating Cu into damascene trenches of various width/space combinations is not larger than 15 nm. The growth rate of Cu grains is faster in the pattern area than in the blanket area. The initiation of the grain growth occurs at the upper corners of the trench plugs. The number density of corners is higher in the pattern area than in the blanket area. The textures of all the specimens except the blanket specimen can be approximated by the {111}<110> texture as a major component and its twin components {115}<110> and {115}<141> as minor ones. The texture of the deposit on blanket wafer was approximated by a <111>//ND texture, which inherited from Cu seed layer. The self-annealing textures of the 200 nm/200 nm and 240 nm/200 nm width/space patterned trenches were approximated by a major {111}<110> component and a minor {115}<110> and {115}<141> components, whereas the texture of the 1000 nm/200 nm width/space specimen was approximated by a major {111}<112> component and a minor {115}<552> component, which is a twin component of {111}<112>. The textures of the 500 nm/200 nm, 2000 nm/200 nm, 500 nm/500 nm, and 500 nm/1000 nm specimens are seen to be mixtures of the {111}<110> and {111}<112> orientations, contributions of which vary with specimen. The 4- and 6-μm-wide specimens showed textures which could be approximated by mixtures of diffused {111}<110> and {111}<112> components. The textures measured over the over-plated layer were similar to those of the CMP-specimens. The annealing texture is determined by the strain energy minimization.

The overall and matrix textures of nanocrystalline Cu films deposited by DC sputtering at room temperature onto amorphous SiN_x/Si TEM grids with a viewable area of 100x100 μm^2 are dominated by <110>//ND, but <100> //ND grains and a smaller fraction of <111>//ND grains grow abnormally by elastic strain energy minimization and by surface energy minimization. After annealing at 125 and 300°C, AGG develops strong <112>//ND component by the <100>// ND grains undergoing plastic deformation. Out of grains which have higher *Tf*s and are still in the elastic regime, those with the lowest biaxial elastic modulus (i.e., <112>//ND) would grow at the expense of the surrounding grains. At 500°C, the major AGG texture component becomes <111>//ND by surface energy minimization.

Acknowledgements

This study was supported by the Basic Science Research Program through the National Research Foundation of Korea (NRF) funded by the Ministry of Education (NRF-2013R1A1A2005181) and RIAM.

Author details

Dong Nyung Lee* and Sung Bo Lee*

*Address all correspondence to: dnlee@snu.ac.kr; bolee@snu.ac.kr

Department of Materials Science and Engineering, and RIAM, Seoul National University, Seoul, Republic of Korea

References

[1] Lee DN, Han HN. Recrystallization textures of metals and alloys. In: Wilson P. (ed). Materials Science. InTech; 2013. http://www.intechopen.com/articles/show/title/recrystallization-textures-of-metals-and-alloys

[2] Lee DN, Lee H-J. Effect of stresses on the evolution of annealing textures in Cu and Al interconnects. Journal of Electronic Materials 2003;32 1012-1022.

[3] Shin H-J, Jeong H-T, Lee DN. Deformation and annealing textures of silver wire. Materials Science and Engineering 2000;A279 244-253.

[4] Abbruzzese G, Lücke K. A theory of texture controlled grain growth-I. Derivation and general discussion of the model. Acta Metallurgica 1986;34 905-914.

[5] Hillert M. On the theory of normal and abnormal grain growth. Acta Metallurgica 1965;13 227-238.

[6] Abbruzzese G. Computer simulated grain growth stagnation. Acta Metallurgica 1985;33 1329-1337.

[7] Eichelkraut H, Abbruzzese G, Lücke K. A theory of texture controlled grain growth-II. Numerical and analytical treatment of grain growth in the presence of two texture components. Acta Metallurgica 1988;36 55-68.

[8] Aleshin AN, Aristov VY, Bokstein BS, Shvindlerman LS. Kinetic properties of <111> tilt boundaries in aluminium. Physica Status Solidi 1978;A45 359-366.

[9] Wolf D. Structure-energy correlation for grain boundaries in F.C.C. metals-III. Symmetrical tilt boundaries. Acta Metallurgica et Materialia 1990;38 781-790.

[10] Grant E, Juul Jensen D, Ralph B, Hansen N. Texture development in pure copper. In: Brakman CM, Jongenburger P, Mittemeijer EJ (eds.). Seventh International Conference on Textures of Materials: proceedings of ICOTOM 7. Noordwijkerhout, The Netherlands: Netherlands Society for Materials Science; 1984.

[11] Inakazu N, Kaneno Y, Inoue H. Fiber texture formation and mechanical properties in drawn fine copper wire. Materials Science Forum 1994;157-162 715-720.

[12] Humphreys FJ, Hatherly M. Recrystallization and Related Annealing Phenomena. Pergamon Press; 1995.

[13] Park H, Lee DN. The evolution of annealing textures in 90 pct drawn copper wire. Metallurgical and Materials Transactions 2003;34A 531-541.

[14] Shvindlerman LS, Gottstein G, Molodov DA, Sursaeva VG. Triple junction motion in metals. In: Gottstein G, Molodov DA (eds.), Recrystallization and Grain Growth: proceedings of The First Joint International Conference on Recrystallization and Grain Growth. RWTH Aachen, Germany: Springer-Verlag; 2001.

[15] Porter DA, Eastering KE. Phase Transformations in Metals and Alloys. London: Champman & Hall; 1992.

[16] Harase J. Shimizu R. Dingley DJ. Texture evolution in the presence of precipitates in Fe−3% Si alloy. Acta Metallurgica et Materialia 1991;39 763-770.

[17] Doherty RD, Hughes DA, Humphreys FJ, Jonas JJ, Juul Jensen D, Kassner ME, King WE, McNelley TR, McQeen HJ, Rollett AD. Current issues in recrystallization: a review. Materials Science Engineering 1997;A238 219-274.

[18] Hayakawa Y, Muraki M, Szpunar JA. The changes of grain boundary character distribution during the secondary recrystallization of electrical steel. Acta Metallurgica 1998;46 1063-1073.

[19] Gottstein G, Shvindlerman LS. Grain Boundary Migration in Metals, Boca Raton: CRC Press; 1999. p. 203.

[20] Molodov DA. Grain boundary character – a key factor for grain boundary control. In: Gottstein G, Molodov DA (eds.), Recrystallization and Grain Growth: proceedings of The First Joint International Conference on Recrystallization and Grain Growth. RWTH Aachen, Germany: Springer-Verlag; 2001.

[21] Czerwinski F, Li H, Megret M, Szpunar JA, Clark DG, Erb U. The evolution of texture and grain size during annealing of nanocrystalline Ni-45%Fe electrodeposits. Scripta Materialia 1997; 37 1967-1972.

[22] Park YB, Park J, Ha CS, Yim TH. Texture evolution during the annealing of nanocrystalline permalloy. Materials Science Forum 2002;408-412 919-924.

[23] Park YB, Hong S-H, Ha CS, Lee HY, Yim TH. Orientation dependence of grain growth in a nanocrystalline Ni foil. Materials Science Forum 2002;408-412 931-936.

[24] Lee DN, Hur KH. The evolution of texture during annealing of electroless Ni-Co-P deposits. Scripta Materialia 1999;40 1333-1339.

[25] Lee DN, Hur KH. The evolution of texture during annealing of nanocrystalline electroless Ni alloy deposits. Textures and Microstructures 2000;34 181-195.

[26] Lee DN. Changes in lattice constants and orientation of <100> and <111> oriented grains in nanocrystalline Ni and Ni-Fe electrodeposits after annealing. Materials Science Forum 2007;539-543 149-154.

[27] Metals Handbook. American Society for Metals. 9th edition, Vol. 1, 1979. p.147.

[28] Metals Handbook. American Society for Metals. 9th edition, Vol. 2, 1979. p. 105 for 5086 Al alloy, p. 777 for Ni, p.727 For Cu.

[29] Barrett CS, Massalski TB. Structure of Metals, 3rd edition, McGraw-Hill Book Company; 1966. p. 629.

[30] Metals Handbook. American Society for Metals. 8th edition, Vol. 1, p. 1207.

[31] Hur K-H, Jeong J-H, Lee DN. Effect of annealing on magnetic properties and microstructure of electroless nickel-copper-phosphorous alloy deposits. Journal of Materials Science 1991;26 2037-2044.

[32] Lee DN. Annealing textures of thin films and copper interconnects. Materials Science Forum 2005;475-479 1-8.

[33] Lee DN, Kang S, Yang J. Relation between texture and surface morphology of copper electrodeposits. Plating and Surface Finishing March 1995; 82 76-79.

[34] Carel R, Thompson CV, Frost HJ. Computer simulation of strain energy effects vs surface and interface energy effects on grain growth in thin films. Acta Materialia 1996;44 2479-2494.

[35] Lee DN. Elastic properties of thin films of cubic system. Thin Solid Films 2003;434 183-189.

[36] Lee DN. Corrigendum to [Thin Solid Films 434, 183-189 (2003)], Thin Solid Films 2012;520 3708.

[37] Hearmon RFS. The elastic constants of anisotropic materials—II. Advances in Physics 1956;5 323-382.

[38] Field DP, Sanchez, Jr. JE, Besser PR, Dingley DJ. Analysis of grain-boundary structure in Al–Cu interconnects. Journal of Applied Physics 1997;82 2383-2392.

[39] Field DP, Wang P-H. Development of a preferred grain boundary structure in Al–Cu Interconnects. In: Pond RC, Clark WAT, King AH, Williams DB (eds). Boundaries and Interfaces in Materials: The David A. Smith Symposium, The Minerals, Metals & Materials Society. 1998. pp. 323-328.

[40] Sundquist BE. A direct determination of the anisotropy of the surface free energy of solid gold, silver, copper, nickel, and alpha and gamma iron. Acta Metallurgica et Materialia 1964;12 67-86.

[41] Lee H-J, Kim DI, Ahn JH, Lee DN. Electron backscattered diffraction analysis of copper damascene interconnect for ultralarge-scale integration. Thin Solid Films 2005;474 250-254.

[42] Lingk C, Gross ME. Recrystallization kinetics of electroplated Cu in damascene trenches at room temperature. Journal of Applied Physics 1998;84 5547-5553.

[43] Lee DN, Lee H-J. Self-annealing textures of copper damascene interconnects, Materials Science Forum 2004;467-460 1333-1338.

[44] Lee H-J, Han HN, Lee DN. Annealing texture of copper interconnects for ultralarge scale integration, Journal of Electronic Materials 2005;34 1493-1499.

[45] Kwon K-W, Ryu C, Sinclair R, Wong SS. Evidence of heteroepitaxial growth of copper on beta-tantalum. Applied Physics Letters 1997;71 3069-3071.

[46] Lee DN. Texture development in thin films, Materials Science Forum 2002;408-412 75-94.

[47] Lee DN. Current understanding of annealing texture evolution in thin films and interconnects. Zeitschrift für Metalkunde 2005;96 259-268.

[48] Brongersma SH, Kerr E, Vervoort I, Maex K. Limitations to copper grain growth in narrow trenches. Proc. IEEE Int. Interconnect Technology Conference; 2001. p. 230.

[49] Ueno K, Ritzdorf T, Grace S. Seed layer dependence of room-temperature recrystallization in electroplated copper films. Journal of Applied Physics 1999;86 4930-4935.

[50] Lagrange S, Brongersma SH, Judelewicz M, Saerens A, Vervoort L, Richard E, Palmans R, Maex K. Self-annealing characterization of electroplated copper films. Microelectronic Engineering 2000;50 449-457.

[51] Teh WH, Koh LT, Chen SM, Xie J, Li CY, Foo PD. Study of microstructure and resistivity evolution for electroplated copper films at near-room temperature. Microelectronics Journal 2001;32 579-585.

[52] Reeber RR, Wang K. Thermal expansion and lattice parameters of group IV semiconductors. Materials Chemistry and Physics 1996;46, 259-264.

[53] Hellwege KH, Hellwege AM (eds.). Landolt-Börnstein: Numerical Data and Functional Relationships in Science and Technology. Group-III, vol.1. New York: Springer; 1966.

[54] Zhao J-H, Ryan T, Ho PS, Mckerrow AJ, Shih W-Y. Measurement of elastic modulus, Poisson ratio, and coefficient of thermal expansion of on-wafer submicron films. Journal of Applied Physics 1999;85 6421-6424.

[55] Zhao J-H, Du Y, Morgen M, Ho PS. Simultaneous measurement of Young's modulus, Poisson ratio, and coefficient of thermal expansion of thin films on substrates. Journal of Applied Physics 2000;87 1575-1577.

[56] Brandes EA, Brook GB (eds.). Smithells Metals Reference Book. 7th edition, Butterworth-Heinemann; 1999.

[57] Lynch CT (ed.). CRC Handbook of Materials Science. vol. II, Boca Raton, FL: CRC Press; 1975.

[58] Shen Y-L, Suresh S, Blech IA. Stresses, curvatures, and shape changes arising from patterned lines on silicon wafers. Journal of Applied Physics 1996;80 1388-1398.

[59] Lee SB, Kim D-I, Hong S-H, Lee DN. Texture evolution of abnormal grains with post-deposition annealing temperature in nanocrystalline Cu thin films. Metallurgical and Materials Transactions A 2013;44 152-162.

[60] Lee DN. A model for development of orientation of vapor deposits. Journal of Materials Science 1989;24 4375-4378.

[61] Lee DN. Textures and structures of vapor deposits. Journal of Materials Science 1999;34 2575-2582.

[62] Kwatera A. Thin CVD layers of carbon-doped silicon nitride on quartz. Ceramics International 1989;15 65-129.

[63] Chang YA, Himmel L. Temperature dependence of the elastic constants of Cu, Ag, and Au. Journal of Applied Physics 1966;37 3567-3572.

[64] Detavernier C, Deduytsch D, Van Meirhaeghe RL, DeBaerdemaeker J, Dauwe C. Room-temperature grain growth in sputter-deposited Cu films. Applied Physics Letters 2003;82 1863-1865.

[65] Chin GY, Mammel WL. Computer solutions of the Taylor analysis for axisymmetric flow. Transactions of the Metallurgical Society of AIME 1967;239 1400-1405.

[66] Lee DN, Han HN, Kim S-J. Rolling and annealing textures of silver sheets. Proceedings of ICOTOM 15, Symposium 10, TMS, Pittsburgh; 2008.

[67] Kim S-J, Han HN, Jeong H-T, Lee DN. Evolution of the {110}<110> texture in silver sheets. Materials Research. Innovations 2011;15 (Suppl.1) s390-s394.

[68] Oh KH, Park SM, Koo YM, Lee DN. Thermomechanical treatment for enhancing gamma fiber component in recrystallization texture of copper-bearing bake hardening steel. Materials Science and Engineering 2011;A528 6455-6462.

[69] Merriman CC, Field DP, Trivedi P. Orientation dependence of dislocation structure evolution during cold rolling of aluminum. Materials Science and Engineering 2008;A494 28-35.

[70] Longworth HP, Thompson CV. Abnormal grain growth in aluminum alloy thin films. Journal of Applied Physics 1991;69 3929-3940.

[71] Taylor GI. Plastic strain in metals. Journal of the Institute of Metals 1938;62 307-324.

[72] Bishop JFW, Hill R. A theory of the plastic distortion of a polycrystalline aggregate under combined stresses. Philosophical Magazine 1951;42 414-427.

[73] Bishop JFW, Hill R. Atheoretical derivation of the plastic properties of polycrystalline face-centered metal. Philosophical Magazine 1951;42 1298-1307.